Event-Based Communication Strategies for Collaborative Inertial Radio SLAM

JOSHUA J. MORALES, Member, IEEE
JOE J. KHALIFE, Member, IEEE
ZAHER M. KASSAS, Senior Member, IEEE
The Ohio State University, Columbus, OH USA

Event-based communication strategies for vehicles navigating by aiding their inertial navigation systems (INSs) with terrestrial signals of opportunity (SOPs) are developed. The following problem is considered. Multiple navigating vehicles with access to global navigation satellite system (GNSS) signals are aiding their on-board INSs with GNSS pseudoranges. While navigating, vehicle-mounted receivers draw pseudorange measurements from terrestrial SOPs with unknown emitter positions and unknown and unsynchronized clocks. The vehicles share INS data and SOP pseudoranges to collaboratively estimate the SOPs' states through an extended Kalman filter (EKF). After some time, GNSS signals become unavailable, at which point the navigating vehicles use shared INS and SOP information to continue navigating in a collaborative inertial radio simultaneous localization and mapping (CIRSLAM) framework. Two event-based communication strategies to share this information are developed, where instead of sharing information at a fixed-rate when measurements become available, information is only shared whenever any vehicle's position error could violate a user-specified position error threshold with some desired probability. Simulation results are presented demonstrating the tradeoff between localization performance and the accumulated transmitted data when the event-based transmission scheme is employed versus sharing data at the fixed-rate. Experimental results are presented demonstrating two unmanned aerial vehicles (UAVs) navigating in a CIRSLAM framework with SOP pseudoranges drawn from terrestrial cellular towers. The event-based communication scheme reduced the cumulative communicated data by 86.6% compared to a fixed-rate scheme, while maintaining the specified error constraint.

Manuscript received 4 July 2021; revised 11 December 2021, 30 March 2022, 18 July 2022, and 17 August 2022; accepted 25 August 2022. Date of publication 8 November 2022; date of current version 12 April 2023.

DOI. No. 10.1109/TAES.2022.3220722

Refereeing of this contribution was handled by R. Yang.

This work was supported in part by the the Office of Naval Research (ONR) under Grant N00014-19-1-2511 and in part by the National Science Foundation (NSF) under Grant 1929965 and Grant 1929571.

Authors' addresses: Joshua J. Morales was with the University of California Irvine, CA 92697, USA and is now with StarNav LLC Riverside, CA 92501, USA, E-mail: (joshua.morales@ieee.org); Joe J. Khalife was with the University of California Irvine, CA 92697, USA, E-mail: (khalifej@uci.edu); Zaher M. Kassas is with the Department of Electrical and Computer Engineering, The Ohio State University, Columbus, OH 43210, USA, E-mail: (zkassas@ieee.org). *(Corresponding author: Zaher M. Kassas.)*

I. INTRODUCTION

Today's vehicular navigation systems extract position information from a suite of diverse and complementary onboard sensors. For example, a global navigation satellite system (GNSS) receiver provides stable absolute position information and an inertial measurement unit (IMU) and other dead reckoning sensors (e.g., wheel encoders) provide short-term accurate information [1], [2]. After prolonged periods of GNSS signal unavailability, the position solution degrades to unsafe levels as error-corrupted dead reckoning information is integrated without correction from an absolute position information source.

Vehicle-mounted sensors (e.g., cameras [3], [4] or lidar [5], [6]) can reduce IMU drift during GNSS unavailability by tracking features in the environment (e.g., walls, light poles, trees, etc.) and then inferring the vehicle's relative motion with respect to the features via a simultaneous localization and mapping (SLAM) framework [7]. However, after extended periods of time without GNSS aiding corrections, the vehicles' position estimate will still drift due to the accumulation of sensor errors (e.g., camera scale factor [8] and lidar range errors due to dust and water particles [9]).

Over the past decade, signals of opportunity (SOPs) [10]; such as AM/FM radio [11], cellular [12], [13], [14], [15], [16], [17], [18], digital television [19], [20], [21], and low Earth orbit (LEO) satellite signals [22], [23], [24], [25]; have been studied and demonstrated as an effective backup or alternative source of absolute positioning information, providing corrections to an inertial navigation system (INS) in the absence of GNSS signals [26], [27]. SOPs posses several desirable characteristics for vehicular navigation: 1) available in most environments of interest, 2) difficult to jam all SOPs, since their signals are scattered throughout the spectrum, 3) produce low geometric dilution of precision, since their transmitters are geometrically diverse, 4) signal reception with carrier-to-noise ratio that is often tens of decibels (dBs) higher than that of GNSS signals, 5) free to use with SOP navigation receivers that do not require network subscriptions, and 6) no deployment cost, since their infrastructure is already operational and maintained by service providers. Even if GNSS pseudoranges are reliable, adding terrestrial SOP pseudorange measurements to the navigation filter will significantly reduce positioning errors for land, sea, and air vehicles, primarily due to a reduction of the inherently large GNSS vertical dilution of precision (VDOP) [28].

However, unlike GNSS, whose satellites' positions and clock states are known to the navigating vehicle, the positions and clock states of SOP transmitters are typically unknown *a priori* and must be estimated [29], [30], [31]. Extend Kalman-filter based radio SLAM frameworks have been developed to iteratively estimate the SOPs' states

along with the states of the navigating vehicle [27]. Radio SLAM is similar to traditional SLAM used with cameras and lidar, except the radio SLAM problem has unique complexities, since it must deal with stochastic and dynamic SOP clock biases and drifts.

Whether cameras, lidar, or SOPs are used as an INS aiding source, collaboration between multiple vehicles can improve vehicle positioning performance compared to standalone navigation by sharing and fusing their individual sensor information [32], [33], [34], [35], [36]. However, the tradeoff for this performance improvement is increased system cost, complexity, and communication burden. Communication of inertial data particularly comes with a large communication burden due to the substantial amount of IMU data produced by each vehicle, the communication of which is required to maintain proper intervehicle correlations for consistent EKF-produced estimates. To reduce the communication burden associated with transmitting IMU data, vehicles can transmit state estimates and associated covariances. To deal with unknown intervehicle correlations, covariance intersection fusion has been a popular method of choice to approximate the unknown correlations [32], [34], [37], [38], [39], [40], [41], [42]. While covariance intersection avoids tracking the actual intervehicle correlations, the produced estimation error covariance still tend to be larger than the actual covariance of the errors. In contrast to prior approaches, this article maintains intervehicle correlations and deals with the communication burden by determining the minimal sufficient INS information that must be communicated to maintain consistent estimates. An event-based communication scheme is developed, which minimizes the amount of communicated information by transmitting data only if an event of interest is triggered [43], [44]. In the proposed approach, measurements are discarded unless an event is triggered to maintain state estimation consensus among the filters running at each vehicle. A relaxation of this assumption can be readily achieved in which local measurements at each of the vehicles are processed between event triggers, whereby covariance intersection is performed after an event is triggered [34].

In recent years, event-based communication has been studied in several contexts (see [45] and references therein). These studies have led to different event-triggering tests, such as: 1) level-triggering, which compares the amplitude of a signal versus a predefined threshold [46]; 2) average estimation error covariance, which checks the average of the time-history of the trace of the estimation error covariance [47]; 3) state difference, which uses the difference between a vehicle's current state and the last transmitted state; 4) residual-based, which checks the difference between the actual and predicted measurement [48]; 5) innovation variance-based tests [43], and 6) weighted difference of sequential measurements [49].

While several event-triggering tests have been developed, the development of event-based tests in the contexts of collaborative SLAM using an INS has not been considered. In [50], an event-based scheme was developed for a distributed filter; however, it was studied using a simplified linear dynamics model. In [51], an event-based scheme was developed for cooperative SLAM for a nonlinear dynamics model in two dimensions and used covariance intersection to maintain intervehicle cross-correlations. This article develops an event-based scheme for a CIRSLAM framework, in which multiple vehicles estimate the *unknown* states of terrestrial SOPs along with the states of navigating vehicles using shared SOP and INS information.

The CIRSLAM framework was originally presented in [52], which compared vehicle positioning errors when using time of arrival (TOA) with using time difference of arrival measurements. This article uses TOA measurements in the CIRSLAM framework and determines when these measurements should be communicated to collaborators. In [49], measurements are transmitted to a central relay station for event testing to determine if the measurements should be relayed to distributed nodes. In contrast, this article develops an event-based scheme, where event testing is conducted locally in a distributed fashion, where vehicles only exchange information if the norm of the estimation error will violate a user-specified position error threshold with some desired probability. Two norms important for vehicular navigation are considered: two-norm, which tests absolute positioning error and infinity-norm, which tests the largest error in any coordinate direction. The developed theory and algorithms are evaluated through high-fidelity simulations and experimental results with IMU data and cellular SOPs. It is important to emphasize that while the EKF equations presented in this article support the use of SOPs, the event-based tests developed in this article are independent of them and can be applied to other multisensor integrated navigation applications.

The rest of this article is organized as follows. Section II provides an overview of the CIRSLAM framework as well as the event-based communication strategies studied in this article. Section III describes the dynamics model of the SOPs and navigating vehicles as well as the receivers' measurement model. Section IV describes the EKF-based CIRSLAM framework. Section VI develops an event-based communication scheme. Section VI presents simulation results comparing an event-based information communication scheme with a fixed-rate scheme. Section VII presents experimental results of collaborating unmanned aerial vehicals (UAVs) using cellular SOPs to aid their INSs. Finally, Section VIII concludes this article.

II. OVERVIEW OF CIRSLAM FRAMEWORK AND PROBLEM STATEMENT

A high-level block diagram of the CIRSLAM framework is illustrated in Fig. 1. This framework enables a team of navigating vehicles to share INS data, GNSS pseudoranges, and SOP pseudoranges. During the time between measurement epochs, each vehicle uses its IMU data and clock models to perform an EKF time update and then packages INS information into $\mathbf{\Lambda}_n$ to share it with the other navigating vehicles. At each measurement epoch, receivers equipped on each vehicle produce pseudoranges to GNSS

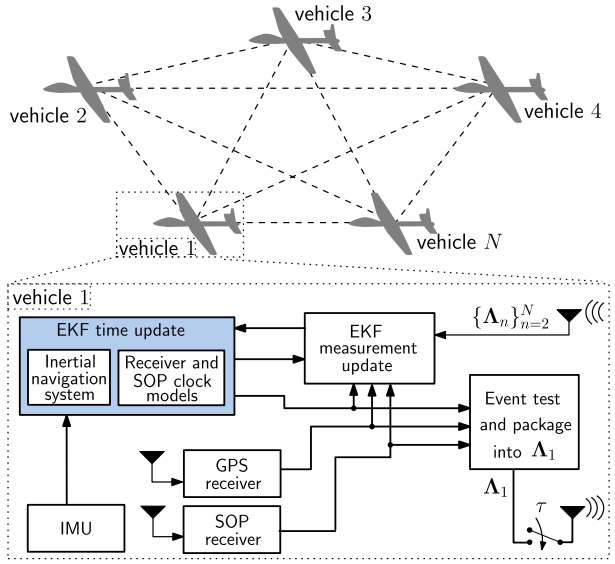

Fig. 1. High-level diagram of an EKF-based CIRSLAM using GNSS (when available) and SOP pseudoranges. All drawn SOP pseudoranges and INS data are fused through an EKF running on each vehicle. This fusion takes place by packaging information into $\{\mathbf{\Lambda}_n\}_{n=1}^N$ and broadcasting them using an event-based strategy, which employs a mechanism to close τ only when needed.

satellites (when GNSS signals are available) and pseudoranges to SOP transmitters. This information is then sent to a local EKF measurement update step and is packaged into $\mathbf{\Lambda}_n$ along with the INS information. Typically, EKFs operate at a fixed rate of the measurement epoch, which would require the transmission of $\mathbf{\Lambda}_n$ whenever GNSS or SOP pseudoranges are produced. This article is concerned with alleviating the communication burden by developing event-based strategy, which only triggers transmission and the EKF update so to achieve a user-specified position error bound with some desired probability. The probability density function of the value that triggers the event is studied to ensure the user-specified values are maintained. A fully connected graph is assumed, i.e., all vehicles are able to communicate with all other vehicles. To prevent transmitting large amounts of IMU data, only the INS state and information to construct the state transition matrix are communicated. This information is used to maintain intervehicle correlations.

III. MODEL DESCRIPTION

In this section, the dynamics model of the SOP transmitters and the vehicles' states as well as the measurement models are provided. These models are used in the subsequent sections for the development of the EKF-based CIRSLAM framework.

A. SOP Dynamics Model

Each SOP will be assumed to emanate from a spatially stationary terrestrial transmitter, and its state vector will consist of its three-dimensional (3-D) position states $\boldsymbol{r}_{\text{sop},m} \triangleq [x_{\text{sop},m},\ y_{\text{sop},m},\ z_{\text{sop},m}]^{\mathsf{T}} \in \mathbb{R}^3$ and clock error states $\boldsymbol{x}_{\text{clk,sop},m} \triangleq [c\delta t_{\text{sop},m},\ c\dot{\delta} t_{\text{sop},m}]^{\mathsf{T}} \in \mathbb{R}^2$, where c is the speed of light, $\delta t_{\text{sop},m}$ is the clock bias, $\dot{\delta} t_{\text{sop},m}$ is the clock drift, $m = 1, \ldots, M$, and M is the total number of SOPs.

The SOP's discretized dynamics are given by

$$\boldsymbol{x}_{\text{sop},m}(k+1) = \mathbf{F}_{\text{sop}}\boldsymbol{x}_{\text{sop},m}(k) + \boldsymbol{w}_{\text{sop},m}(k), \quad k = 1, 2, \ldots,$$
$$\mathbf{F}_{\text{sop}} = \begin{bmatrix} \mathbf{I}_{3\times 3} & \mathbf{0}_{3\times 2} \\ \mathbf{0}_{2\times 3} & \mathbf{F}_{\text{clk}} \end{bmatrix}, \qquad \mathbf{F}_{\text{clk}} = \begin{bmatrix} 1 & T \\ 0 & 1 \end{bmatrix} \tag{1}$$

where $\mathbf{I}_{n\times n}$ denotes the $n \times n$ identity matrix, $\mathbf{0}_{m\times n}$ denotes the $m \times n$ matrix of zeros, T is the constant sampling interval, $\boldsymbol{x}_{\text{sop},m} = \left[\boldsymbol{r}_{\text{sop},m}^{\mathsf{T}},\ \boldsymbol{x}_{\text{clk,sop},m}^{\mathsf{T}}\right]^{\mathsf{T}} \in \mathbb{R}^5$, and $\boldsymbol{w}_{\text{sop},m} \in \mathbb{R}^5$ is the process noise, which is modeled as a discrete-time zero-mean white noise sequence with covariance $\mathbf{Q}_{\text{sop},m} = \text{diag}\left[\mathbf{0}_{3\times 3},\ c^2\mathbf{Q}_{\text{clk,sop},m}\right]$, where

$$\mathbf{Q}_{\text{clk,sop},m} = \begin{bmatrix} S_{w_{\delta t_{\text{sop},m}}} T + S_{w_{\dot{\delta} t_{\text{sop},m}}} \frac{T^3}{3} & S_{w_{\dot{\delta} t_{\text{sop},m}}} \frac{T^2}{2} \\ S_{w_{\dot{\delta} t_{\text{sop},m}}} \frac{T^2}{2} & S_{w_{\dot{\delta} t_{\text{sop},m}}} T \end{bmatrix}.$$

The terms $S_{w_{\delta t_{\text{sop},m}}}$ and $S_{w_{\dot{\delta} t_{\text{sop},m}}}$ are the clock bias and drift process noise power spectra, respectively, which can be related to the power-law coefficients, $\{h_{\alpha,\text{sop},m}\}_{\alpha=-2}^{2}$, which have been shown through laboratory experiments to characterize the power spectral density of the fractional frequency deviation of an oscillator from nominal frequency according to $S_{\delta t_{\text{sop},m}} \approx \frac{h_{0,\text{sop},m}}{2}$ and $S_{\dot{\delta} t_{\text{sop},m}} \approx 2\pi^2 h_{-2,\text{sop},m}$ [53].

B. Vehicle Dynamics Model

Let $\{b_n\}$ denote a body frame fixed at the nth navigating vehicle, where $n = 1, \ldots, N$ and N is the total number of navigating vehicles, and let $\{g\}$ denote a global frame, e.g., the Earth-centered inertial (ECI) frame [54]. Moreover, let $\boldsymbol{\theta}_{b_n} \in \mathbb{R}^3$ represent the 3-D orientation vector of the body frame with respect to the global frame and $\boldsymbol{r}_{b_n} \in \mathbb{R}^3$ the 3-D position vector of the nth navigating vehicle expressed in $\{g\}$. Given the nth INS's true 3-D rotational rate vector ${}^{b_n}\boldsymbol{\omega} \in \mathbb{R}^3$ in the body frame and its 3-D acceleration ${}^{g}\boldsymbol{a}_{b_n} \in \mathbb{R}^3$ in the global frame, the standard kinematics equations can be expressed in continuous time as

$$\dot{\boldsymbol{\theta}}_{b_n}(t) = {}^{b_n}\boldsymbol{\omega}(t) \tag{2}$$
$$\ddot{\boldsymbol{r}}_{b_n}(t) = {}^{g}\boldsymbol{a}_{b_n}(t). \tag{3}$$

In the rest of this article, the 3-D orientation vector of the body frame with respect to the global frame will be represented by the 4-D quaternion vector ${}^{b_n}_{g}\bar{\boldsymbol{q}} \in \mathbb{R}^4$.

1) *IMU Measurement Model:* The IMU on the nth navigating vehicle contains a triad-gyroscope and a triad-accelerometer, which produce measurements ${}^{n}\boldsymbol{z}_{\text{imu}} \triangleq [{}^{n}\boldsymbol{\omega}_{\text{imu}}^{\mathsf{T}},\ {}^{n}\boldsymbol{a}_{\text{imu}}^{\mathsf{T}}]^{\mathsf{T}}$ of the angular rate and specific force, which are modeled using strapdown equations as

$${}^{n}\boldsymbol{\omega}_{\text{imu}}(k) = {}^{b_n}\boldsymbol{\omega}(k) + \boldsymbol{b}_{\text{gyr},n}(k) + \boldsymbol{n}_{\text{gyr},n}(k) \tag{4}$$
$${}^{n}\boldsymbol{a}_{\text{imu}}(k) = \mathbf{R}\left[{}^{b_n}_{g}\bar{\boldsymbol{q}}(k)\right]\left({}^{g}\boldsymbol{a}_{b_n}(k) - {}^{g}\boldsymbol{g}_n(k)\right) + \boldsymbol{b}_{\text{acc},n}(k) + \boldsymbol{n}_{\text{acc},n}(k) \tag{5}$$

where $\mathbf{R}[{}^{b_n}_{g}\bar{\boldsymbol{q}}]$ is the equivalent rotation matrix of ${}^{b_n}_{g}\bar{\boldsymbol{q}}$ (see Appendix A); ${}^{g}\boldsymbol{g}_n$ is the acceleration due to gravity acting on the

nth navigating vehicle in the global frame; $\boldsymbol{b}_{\text{gyr},n} \in \mathbb{R}^3$ and $\boldsymbol{b}_{\text{acc},n} \in \mathbb{R}^3$ are the gyroscope and accelerometer biases, respectively; $\boldsymbol{n}_{\text{gyr},n}$ and $\boldsymbol{n}_{\text{acc},n}$ are measurement noise vectors, which are modeled as zero-mean white noise sequences with covariances $\mathbf{Q}_{\boldsymbol{n}_{\text{gyr},n}}$ and $\mathbf{Q}_{\boldsymbol{n}_{\text{acc},n}}$, respectively; and k is the sample counter which represents the time instances IMU data is available according to $t = kT_{\text{imu}}$, for an IMU sampling period T_{imu}.

2) *INS State Kinematics:* The gyroscope and accelerometer biases in (4)–(5) are dynamic and stochastic; hence, they must be estimated in the EKF as well. As such, the INS 16-state vector is given by

$$\boldsymbol{x}_{\text{ins},n} = \left[{}^{b_n}_{g}\bar{\boldsymbol{q}}^{\mathsf{T}}, \quad \boldsymbol{r}_{b_n}^{\mathsf{T}}, \quad \dot{\boldsymbol{r}}_{b_n}^{\mathsf{T}}, \quad \boldsymbol{b}_{\text{gyr},n}^{\mathsf{T}}, \quad \boldsymbol{b}_{\text{acc},n}^{\mathsf{T}} \right]^{\mathsf{T}} \in \mathbb{R}^{16}$$

where $\dot{\boldsymbol{r}}_{b_n} \in \mathbb{R}^3$ is the 3-D velocity of the navigating vehicle. The INS states evolve in time according to

$$\boldsymbol{x}_{\text{ins},n}(k+1) = \boldsymbol{f}_{\text{ins}}\left[\boldsymbol{x}_{\text{ins},n}(k), {}^{b_n}\boldsymbol{\omega}(k), {}^{g}\boldsymbol{a}_{b_n}(k) \right]$$

where $\boldsymbol{f}_{\text{ins}}$ is a vector-valued function of standard strapdown kinematic equations, which discretizes (2)–(3) by integrating ${}^{b_n}\boldsymbol{\omega}$ and ${}^{g}\boldsymbol{a}_{b_n}$ to produce ${}^{b_n}_{g}\bar{\boldsymbol{q}}(k+1)$, $\boldsymbol{r}_{b_n}(k+1)$, and $\dot{\boldsymbol{r}}_{b_n}(k+1)$, and uses a velocity random walk model for the biases, which is given by

$$\boldsymbol{b}_{\text{gyr},n}(k+1) = \boldsymbol{b}_{\text{gyr},n}(k) + \boldsymbol{w}_{\text{gyr},n}(k) \tag{6}$$

$$\boldsymbol{b}_{\text{acc},n}(k+1) = \boldsymbol{b}_{\text{acc},n}(k) + \boldsymbol{w}_{\text{acc},n}(k) \tag{7}$$

where $\boldsymbol{w}_{\text{gyr},n}$ and $\boldsymbol{w}_{\text{acc},n}$ are process noise vectors that drive the in-run bias variation (or bias instability) and are modeled as white noise sequences with covariance $\mathbf{Q}_{\boldsymbol{w}_{\text{gyr},n}}$ and $\mathbf{Q}_{\boldsymbol{w}_{\text{acc},n}}$, respectively. The INS state vector is augmented with the navigating vehicle-mounted receiver's clock state vector $\boldsymbol{x}_{\text{clk,r},n} \in \mathbb{R}^2$ to obtain the nth navigating vehicle's state vector $\boldsymbol{x}_{\text{r},n} = [\boldsymbol{x}_{\text{ins},n}^{\mathsf{T}}, \boldsymbol{x}_{\text{clk,r},n}^{\mathsf{T}}]^{\mathsf{T}} \in \mathbb{R}^{18}$.

REMARK While this article develops an aided INS using an inertial frame (e.g., the ECI frame), other forms of the function $\boldsymbol{f}_{\text{ins}}$ may be used in the CIRSLAM framework, depending on the navigation frame chosen, the mechanization type, and the INS error model used.

3) *Receiver Clock State Dynamics:* The nth vehicle-mounted receiver's clock states evolve according to

$$\boldsymbol{x}_{\text{clk,r},n}(k+1) = \mathbf{F}_{\text{clk}}\boldsymbol{x}_{\text{clk,r},n}(k) + \boldsymbol{w}_{\text{clk,r},n}(k) \tag{8}$$

where $\boldsymbol{w}_{\text{clk,r},n} \in \mathbb{R}^2$ is the process noise vector, which is modeled as a discrete-time zero-mean white noise sequence with covariance $\mathbf{Q}_{\text{clk,r},n}$, which has an identical form to $\mathbf{Q}_{\text{clk,sop},m}$, except that $S_{w_{\delta t_{\text{sop},m}}}$ and $S_{w_{\dot{\delta}t_{\text{sop},m}}}$ are now replaced with receiver-specific spectra $S_{w_{\delta t_{\text{r},n}}}$ and $S_{w_{\dot{\delta}t_{\text{r},n}}}$, respectively.

C. Pseudorange Measurement Model

The pseudorange measurements made by the nth receiver on the m^{th} SOP, after discretization and mild approximations discussed in [29], are modeled as

$$\begin{aligned} {}^{n}z_{\text{sop},m}(j) &= \|\boldsymbol{r}_{b_n}(j) - \boldsymbol{r}_{\text{sop},m}\|_2 \\ &\quad + c \cdot \left[\delta t_{\text{r},n}(j) - \delta t_{\text{sop},m}(j)\right] + {}^{n}v_{\text{sop},m}(j) \end{aligned} \tag{9}$$

where ${}^{n}v_{\text{sop},m}$ is the measurement noise, which is modeled as a discrete-time zero-mean white Gaussian sequence with variance ${}^{n}\sigma^2_{\text{sop},m}$ and $j \in \mathbb{N}$ represents the time index at which $\{{}^{n}z_{\text{sop},m}\}_{n=1}^{N}$ is available, which could be *aperiodic*. Note that for measurement variables, the upper-left subscript is used to denote the vehicle identity number drawing the measurement and the lower-right subscript is used for the transmitter that the measurement is drawn from. The pseudorange measurement made by the nth receiver on the lth GNSS SV, after compensating for ionospheric and tropospheric delays, is related to the navigating vehicle's states by

$$\begin{aligned} {}^{n}z_{\text{sv},l}(j) &= \|\boldsymbol{r}_{b_n}(j) - \boldsymbol{r}_{\text{sv},l}(j)\|_2 \\ &\quad + c \cdot \left[\delta t_{\text{r},n}(j) - \delta t_{\text{sv},l}(j)\right] + {}^{n}v_{\text{sv},l}(j) \end{aligned} \tag{10}$$

where ${}^{n}z_{\text{sv},l} \triangleq {}^{n}z'_{\text{sv},l} - c\delta t_{\text{iono}} - c\delta t_{\text{tropo}}$; δt_{iono} and δt_{tropo} are the ionospheric and tropospheric delays, respectively; ${}^{n}z'_{\text{sv},l}$ is the uncorrected pseudorange; and ${}^{n}v_{\text{sv},l}$ is the measurement noise, which is modeled as a discrete-time zero-mean white Gaussian sequence with variance ${}^{n}\sigma^2_{\text{sv},l}$; and $l = 1, \ldots, L$, where L is the total number of GNSS SVs.

IV. COLLABORATIVE INERTIAL RADIO SIMULTANEOUS LOCALIZATION AND MAPPING (CIRSLAM)

This section develops the EKF-based CIRSLAM framework, illustrated in Fig. 1, to fuse pseudorange measurements from unknown SOPs and GNSS (if available) to aid each navigating vehicle's INS. A method to efficiently share INS data between collaborators is also discussed.

A. EKF-Based CIRSLAM Framework

In a CIRSLAM framework, the states of the SOPs are simultaneously estimated along with the states of the navigating vehicles. This can be achieved through an EKF with state vector

$$\boldsymbol{x} \triangleq \left[\boldsymbol{x}_{\text{r},1}^{\mathsf{T}}, \ldots, \boldsymbol{x}_{\text{r},N}^{\mathsf{T}}, \boldsymbol{x}_{\text{sop},1}^{\mathsf{T}}, \ldots, \boldsymbol{x}_{\text{sop},M}^{\mathsf{T}}\right]^{\mathsf{T}}.$$

The EKF produces an estimate, given by $\hat{\boldsymbol{x}}(k|j) \triangleq \mathbb{E}[\boldsymbol{x}(k)|\boldsymbol{Z}^j]$ of $\boldsymbol{x}(k)$, where $\mathbb{E}[\,\cdot\,|\,\cdot\,]$ is the conditional expectation operator, $\boldsymbol{Z}^j \triangleq \{\boldsymbol{z}(i)\}_{i=1}^{j}$, $\boldsymbol{z}$ is a vector of INS-aiding measurements (e.g., from GNSS or SOPs), $k \geq j$, and j is the last time-step an INS-aiding measurement was available.

Collaborating navigating vehicles that estimate common states using mutual observations traditionally fuse information (state estimates and/or observations) from each collaborator using one of two main architectures

1) *Centralized*: Each vehicle sends raw sensor data to a central fusion center, which estimates a common state vector and periodically sends the estimate to each vehicle. Centralized architectures produce consistent estimates, i.e., the EKF-produced estimation error covariance matches the covariance of the actual estimation error, since all intervehicle correlations are properly maintained. The drawback is in the large

Algorithm 1: Distributed CIRSLAM Framework.

Given: $\hat{\boldsymbol{x}}(j|j)$ and $\mathbf{P}_{\boldsymbol{x}}(j|j)$, each of the N vehicles conducts the following:

for $n = 1, \ldots, N$

- **Local Prediction:** Locally produce $\hat{\boldsymbol{x}}_{\mathrm{r},n}(k|j)$ using an INS and clock models and $\{\hat{\boldsymbol{x}}_{\mathrm{sop},m}(k|j)\}_{m=1}^{M}$ using SOP dynamics model.
- **Communication:** Package $\hat{\boldsymbol{x}}_{\mathrm{r},n}(k|j)$, pseudorange measurements, and INS data into $\boldsymbol{\Lambda}_n$ and transmit $\boldsymbol{\Lambda}_n$ if τ is closed.
- **Assimilation:** Unpackage $\{\boldsymbol{\Lambda}_i\}_{i=1}^{N} \backslash n$, assemble $\hat{\boldsymbol{x}}(k|j)$, and produce $\mathbf{P}_{\boldsymbol{x}}(k|j)$.
- **Correction:** Perform EKF measurement update to produce $\hat{\boldsymbol{x}}(k|k)$ and $\mathbf{P}_{\boldsymbol{x}}(k|k)$.

end for

amount of raw sensor data that must be communicated to the central fusion center. Furthermore, the central fusion center is a single point of failure for the system.

2) *Distributed*: Each vehicle estimates a copy of the state vector using its own sensor data and then each vehicle shares and fuses these copies using covariance intersection (or one of its variants). Distributed architectures typically require less data transmission between collaborators, since raw sensor data is filtered locally at each vehicle. The drawback is in the difficulty of reaching consensus, i.e., in reaching agreement between the estimate copies, when intervehicle correlations are unknown [55]. While covariance intersection techniques are used to fuse estimates with unknown intervehicle correlations, they typically produce overly conservative estimates, i.e., the EKF-produced estimation error covariance is larger than the actual covariance of the estimation error.

In contrast to traditional centralized and distributed approaches, the approach of the distributed CIRSLAM framework illustrated in Fig. 1 is for each navigating vehicle to monitor the entire state vector $\boldsymbol{x}$, but to distribute the INSs (the EKF time update step) among the navigating vehicles and to optimize how often $\boldsymbol{\Lambda}_n$ is transmitted for aiding corrections (the EKF measurement update step). This approach eliminates a single point of failure, reduces the amount of transmitted data, and with the appropriate transmitted information in $\boldsymbol{\Lambda}_n$, the entire state vector $\boldsymbol{x}$ that is monitored at any particular vehicle will be brought into consensus with the state vector monitored at all other vehicles. These benefits comes at the cost of a larger computational burden for the entire system compared to a traditional centralize approach due to running identical navigation filters at each vehicle. The distributed CIRSLAM framework's operation is summarized in algorithm 1.

B. Local Prediction

Each vehicle only locally produces a prediction of its own state vector $\hat{\boldsymbol{x}}_{\mathrm{r},n}(k|j)$ and of the SOPs' $\{\hat{\boldsymbol{x}}_{\mathrm{sop},m}(k|j)\}_{m=1}^{M}$. The full state prediction $\hat{\boldsymbol{x}}(k|j)$ and the corresponding prediction error covariance $\mathbf{P}_{\boldsymbol{x}}(k|j)$ become available locally during the assimilation step, which is described in Section IV-D.

1) *State Prediction:* To produce $\hat{\boldsymbol{x}}_{\mathrm{r},n}(k|j) = [\hat{\boldsymbol{x}}_{\mathrm{ins},n}^{\mathsf{T}}(k|j), \hat{\boldsymbol{x}}_{\mathrm{clk,r},n}^{\mathsf{T}}(k|j)]^{\mathsf{T}}$, the INS on-board the nth navigating vehicle integrates ${}^{n}\boldsymbol{z}_{\mathrm{imu}}$ between aiding updates to produce a prediction of $\boldsymbol{x}_{\mathrm{ins},n}$. The one-step prediction is given by

$$\hat{\boldsymbol{x}}_{\mathrm{ins},n}(j+1|j) = \boldsymbol{f}_{\mathrm{ins}}\big[\hat{\boldsymbol{x}}_{\mathrm{ins},n}(j|j), {}^{b_n}\hat{\boldsymbol{\omega}}(j), {}^{g}\hat{\boldsymbol{a}}_{b_n}(j)\big] \quad (11)$$

where ${}^{b_n}\hat{\boldsymbol{\omega}}(j)$ and ${}^{g}\hat{\boldsymbol{a}}_{b_n}(j)$ are the estimates of ${}^{b_n}\boldsymbol{\omega}(j)$ and ${}^{g}\boldsymbol{a}_{b_n}(j)$, respectively, obtained from (4)–(5) and $\hat{\boldsymbol{x}}_{\mathrm{ins},n}(j|j)$ [27], and the function $\boldsymbol{f}_{\mathrm{ins}}$ contains standard strapdown INS equations mechanized in an ECI frame, which are described in [56] and [57]. Assuming there are κ time-steps between aiding updates, the navigating vehicle uses IMU data $\{{}^{n}\boldsymbol{z}_{\mathrm{imu}}(i)\}_{i=j}^{k}$ to recursively solve (11) to produce $\hat{\boldsymbol{x}}_{\mathrm{ins}_n}(k|j)$, where $k \equiv j + \kappa$. The vehicle-mounted receiver's κ-step clock state prediction follows from (8) and is given by

$$\hat{\boldsymbol{x}}_{\mathrm{clk,r},n}(k|j) = \mathbf{F}_{\mathrm{clk}}^{\kappa}\hat{\boldsymbol{x}}_{\mathrm{clk,r},n}(j|j)$$

where

$$\mathbf{F}_{\mathrm{clk}}^{\kappa} \triangleq \begin{cases} \mathbf{I}_{2\times 2} & \kappa = 0 \\ \prod_{i=1}^{\kappa} \mathbf{F}_{\mathrm{clk}} & \kappa > 0 \end{cases}$$

The SOPs' κ-step state prediction, which follows from (1), is given by

$$\hat{\boldsymbol{x}}_{\mathrm{sop},m}(k|j) = \mathbf{F}_{\mathrm{sop}}^{\kappa}\hat{\boldsymbol{x}}_{\mathrm{sop},m}(j|j), \qquad m = 1, \ldots, M.$$

2) *Prediction Error Covariance:* Although the prediction error covariance is not produced at this point in the algorithm, its computation is presented here to explain why the cross-correlations are unavailable, which prohibit its production until assimilation, which is discussed in Section IV-D. The κ-step covariance prediction is given by

$$\mathbf{P}_{\boldsymbol{x}}(k|j) = \mathbf{F}(k,j)\mathbf{P}_{\boldsymbol{x}}(j|j)\mathbf{F}^{\mathsf{T}}(k,j) + \mathbf{Q}^{+}(k,j) \quad (12)$$

$$\begin{aligned} \mathbf{F}(k,j) &\triangleq \mathrm{diag}\Big[\mathbf{F}_{\mathrm{r},1}(k,j), \ldots, \mathbf{F}_{\mathrm{r},N}(k,j), \mathbf{F}_{\mathrm{sop}}^{\kappa}, \ldots, \mathbf{F}_{\mathrm{sop}}^{\kappa}\Big] \\ \mathbf{F}_{\mathrm{r},n}(k,j) &\triangleq \mathrm{diag}_{k}\big[\boldsymbol{\Phi}_{\mathrm{ins},n}(k,j), \mathbf{F}_{\mathrm{clk}}^{\kappa}\big] \\ \boldsymbol{\Phi}_{\mathrm{ins},n}(k,j) &\triangleq \prod_{i=j} \boldsymbol{\Phi}_{\mathrm{ins},n}(i) \end{aligned} \quad (13)$$

where $\boldsymbol{\Phi}_{\mathrm{ins},n}(i)$ is the Jacobian of $\boldsymbol{f}_{\mathrm{ins}}$ evaluated at $\hat{\boldsymbol{x}}_{\mathrm{ins},n}(i|j)$. The structure of $\boldsymbol{\Phi}_{\mathrm{ins},n}(i)$ is provided in Appendix A. The matrix $\mathbf{Q}^{+}(k,j)$ is the propagated process noise covariance, which has the form

$$\mathbf{Q}^{+}(k,j) \triangleq \mathrm{diag}\Big[\mathbf{Q}_{\mathrm{r},1}^{+}(k,j), \ldots, \mathbf{Q}_{\mathrm{r},N}^{+}(k,j) \; \mathbf{Q}_{\mathrm{sop},1}^{+}(k,j), \ldots, \mathbf{Q}_{\mathrm{sop},M}^{+}(k,j)\Big]$$

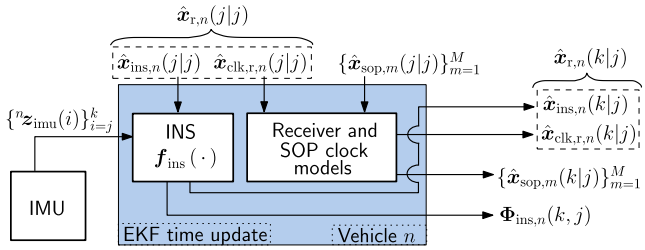

Fig. 2. Local prediction for vehicle n. The inputs are IMU data $\{{}^{n}\boldsymbol{z}_{\mathrm{imu}}(i)\}_{i=j}^{k}$ and the current state estimates $\hat{\boldsymbol{x}}_{\mathrm{r},n}(j|j)$ and $\{\hat{\boldsymbol{x}}_{\mathrm{sop},m}(j|j)\}_{m=1}^{M}$. The outputs are the time updates $\hat{\boldsymbol{x}}_{\mathrm{r},n}(k|j)$ and $\{\hat{\boldsymbol{x}}_{\mathrm{sop},m}(k|j)\}_{m=1}^{M}$ and the Jacobian $\boldsymbol{\Phi}_{\mathrm{ins},n}(k,\,j)$.

$$\mathbf{Q}^{+}_{\mathrm{r},n}(k,\,j) \triangleq \sum_{i=j}^{k} \mathbf{F}_{\mathrm{r},n}(i,\,j)\mathbf{Q}_{\mathrm{r},n}(i)\mathbf{F}^{\mathsf{T}}_{\mathrm{r},n}(i,\,j)$$

$$\mathbf{Q}^{+}_{\mathrm{sop},m}(k,\,j) \triangleq \sum_{i=j}^{k} \mathbf{F}^{(i-j)}_{\mathrm{sop}}\mathbf{Q}_{\mathrm{sop},m}\left[\mathbf{F}^{\mathsf{T}}_{\mathrm{sop}}\right]^{(i-j)}$$

where $\mathbf{Q}_{\mathrm{r},n}(i) \triangleq \mathrm{diag}[\mathbf{Q}_{\mathrm{ins},n}(i),\, c^2\mathbf{Q}_{\mathrm{clk,r},n}]$ and $\mathbf{Q}_{\mathrm{ins},n}$ is the nth navigating vehicle's discrete-time linearized INS process noise covariance. The structure of $\mathbf{Q}_{\mathrm{ins},n}(i)$ is provided in Appendix A. The local prediction for vehicle n is illustrated in Fig. 2.

Note that at this point in the algorithm, the prediction error covariance (12) cannot be computed at vehicle n, $\forall\, n \in \{1, \ldots, N\}$, since all matrices $\{\boldsymbol{\Phi}_{\mathrm{ins},n}(k,\,j)\}_{n=1}^{N}$ are not available at each vehicle. Specifically, the cross-correlation components cannot be computed. In the next section, it is shown what INS information each vehicle transmits, so that the cross-correlation can be computed, enabling the computation of (12) at each vehicle during the assimilation step.

C. Vehicle-to-Vehicle Communication

To produce the prediction error covariance (12) at each vehicle, the matrices $\{\boldsymbol{\Phi}_{\mathrm{ins},n}(k,\,j)\}_{n=1}^{N}$ must be available. It can been seen in Appendix A that the components of these matrices are a function of IMU data from each respective navigating vehicle. Therefore, two possible approaches to make $\{\boldsymbol{\Phi}_{\mathrm{ins},n}(k,\,j)\}_{n=1}^{N}$ available to each vehicle are: 1) each vehicle communicates its raw IMU data or 2) each vehicle communicates the full matrix (13). On one hand, IMU data rates are typically between 100 to 400 Hz, with six floating-point values per data sample. On the other hand, the matrix (13) is in $\mathbb{R}^{15\times 15}$, requiring the transmission of 225 floating-point values every EKF measurement update, which typically takes place between 5 to 10 Hz. These data rates make the transmission of either raw accelerometer and gyroscope data or the matrix (13) undesirable for several reasons: 1) large communication bandwidth requirement when scaling this application to many collaborating vehicles, 2) packet drops due to lossy communication channels, and 3) privacy concerns.

To address this communication burden, instead of transmitting raw IMU data or the full matrix (13) every instant a measurement becomes available, a packet $\boldsymbol{\Lambda}_{\mathrm{ins},n}$ containing minimal sufficient INS information to reconstruct an approximation of (13) is transmitted once per κ-step propagation. The structure of (13) after a κ-step propagation and the packet $\boldsymbol{\Lambda}_{\mathrm{ins},n}$ containing the terms that are needed to reconstruct the approximation are provided in Appendix B. The preconditions for this approximation to be valid are the same assumed for the standard EKF and that the time between transmissions is not too large. The error introduced due to this approximation is dependent on the time between transmissions and the vehicles' dynamics. Higher dynamics applications require a higher transmission rate (smaller time between transmissions). As time between transmissions increase, the approximation (43) accumulates additional error. Specifically, the approximation made on the rotation matrices degrades. This approximation has been shown to introduce only around 1 m of error for transmission periods of around 1 s for fixed-wing drone dynamics [58].

The INS information $\boldsymbol{\Lambda}_{\mathrm{ins},n}$ is packaged inside of $\boldsymbol{\Lambda}_n$, along with other information for each vehicle to produce an EKF update, and then is broadcasted by the nth vehicle at the fixed rate of measurement epochs. The packet $\boldsymbol{\Lambda}_n$ is given by

$$\boldsymbol{\Lambda}_n(k) \triangleq \left\{\hat{\boldsymbol{x}}_{\mathrm{ins},n}(k|j),\, \boldsymbol{\Lambda}_{\mathrm{ins},n}(k,\,j),\, {}^{n}\boldsymbol{z}_{\mathrm{sv}}(k),\, {}^{n}\boldsymbol{z}_{\mathrm{sop}}(k)\right\} \quad (14)$$

where ${}^{n}\boldsymbol{z}_{\mathrm{sv}}$ and ${}^{n}\boldsymbol{z}_{\mathrm{sop}}$ are GNSS and SOP pseudoranges, respectively, which are discussed further for each strategy in the following sections.

D. Assimilation

Assuming a fully connected graph, as in Fig. 1, the packets $\{\boldsymbol{\Lambda}_n(k)\}_{n=1}^{N}$ contain all components of the state prediction to assemble $\hat{\boldsymbol{x}}(k|j)$ and (12). To assemble $\hat{\boldsymbol{x}}(k|j)$, the INS states $\{\hat{\boldsymbol{x}}_{\mathrm{ins},n}(k|j)\}_{n=1}^{N}$ are augmented in the appropriate order with the clocks' and SOPs' states. Note that the clocks' and SOPs' dynamics are linear; therefore, they do not need to be transmitted. Instead, $\mathbf{F}_{\mathrm{clk}}$ and $\mathbf{F}_{\mathrm{sop}}$ are stored at each vehicle for the time update of these states. To assemble (12), the matrix $\mathbf{F}(k,\,j)$ is first assembled by using the information in $\{\boldsymbol{\Lambda}_{\mathrm{ins},n}\}_{n=1}^{N}$ provided in Appendix A. Specifically, the vectors $\boldsymbol{v}_{1,n}$ and $\boldsymbol{v}_{2,n}$ are used to reconstruct the skew-symmetric matrices $\lfloor \boldsymbol{v}_{1,n}\times\rfloor$ and $\lfloor \boldsymbol{v}_{2,n}\times\rfloor$ in (43) through

$$\lfloor \boldsymbol{a}\times\rfloor = \begin{bmatrix} 0 & -a_3 & a_2 \\ a_3 & 0 & -a_1 \\ -a_2 & a_1 & 0 \end{bmatrix}, \quad \boldsymbol{a} \triangleq \begin{bmatrix} a_1 \\ a_2 \\ a_3 \end{bmatrix}. \quad (15)$$

The quaternions $\bar{\boldsymbol{q}}_{1,n}$ and $\bar{\boldsymbol{q}}_{2,n}$ are converted to rotation matrices through

$$\mathbf{R}[\bar{\boldsymbol{q}}] = \mathbf{I}_{3\times 3} - q_4\lfloor \boldsymbol{q}\times\rfloor + 2\lfloor \boldsymbol{q}\times\rfloor^2$$

where $\bar{\boldsymbol{q}} \triangleq [\boldsymbol{q},\, q_0]^{\mathsf{T}} = [q_1,\, q_2,\, q_3,\, q_0]^{\mathsf{T}}$ and q_0 is the real component of the quaternion. Each vehicle may now make the *same* computation in (12). Finally, use ${}^{n}\boldsymbol{z}_{\mathrm{sv}}(k)$ and ${}^{n}\boldsymbol{z}_{\mathrm{sv}}(k)$, to augment the measurements to perform the EKF measurement update and the corresponding corrected estimation error covariance as described follows.

E. EKF Measurement Update

In this section, the EKF-based CIRSLAM measurement update is described. The EKF measurement update will correct the navigating vehicles' INS and clock states given the measurement vector

$$z \triangleq \left[z_{\text{sv}}^{\mathsf{T}},\, z_{\text{sop}}^{\mathsf{T}}\right]^{\mathsf{T}} \tag{16}$$

$$z_{\text{sv}} \triangleq \left[{}^{1}z_{\text{sv}}^{\mathsf{T}}, \ldots, {}^{N}z_{\text{sv}}^{\mathsf{T}}\right]^{\mathsf{T}}, \quad z_{\text{sop}} \triangleq \left[{}^{1}z_{\text{sop}}^{\mathsf{T}}, \ldots, {}^{N}z_{\text{sop}}^{\mathsf{T}}\right]^{\mathsf{T}}$$

$${}^{n}z_{\text{sv}} = \left[{}^{n}z_{\text{sv},1}, \ldots, {}^{n}z_{\text{sv},L}\right]^{\mathsf{T}}, \quad {}^{n}z_{\text{sop}} = \left[{}^{n}z_{\text{sop},1}, \ldots, {}^{n}z_{\text{sop},M}\right]^{\mathsf{T}}.$$

The following correction equations are valid for: GNSS availability ($L > 0$) and GNSS unavailability ($L = 0$). Given a state prediction $\hat{\boldsymbol{x}}(k|j)$, the state update is computed according to the equations provided in Appendix C. The corresponding estimation error covariance is given by

$$\mathbf{P}_{\boldsymbol{x}}(k|k) = \mathbf{P}_{\boldsymbol{x}}(k|j) - \mathbf{L}(k)\mathbf{S}^{-1}(k)\mathbf{L}^{\mathsf{T}}(k)$$

$$\mathbf{L}(k) \triangleq \mathbf{P}_{\boldsymbol{x}}(k|j)\mathbf{H}^{\mathsf{T}}(k) \tag{17}$$

$$\mathbf{S}(k) \triangleq \mathbf{H}(k)\mathbf{L}(k) + \mathbf{R}(k) \tag{18}$$

$$\boldsymbol{v}(k) \triangleq z(k) - \hat{z}(k|j) \tag{19}$$

where $\hat{z}(k|j)$ is a vector containing the predicted GNSS and SOP pseudoranges. The matrix $\mathbf{H}$ is the measurement Jacobian and has the form

$$\mathbf{H} = \begin{bmatrix} \mathbf{H}_{\text{sv,r}} & \mathbf{0}_{NL\times 5M} \\ \mathbf{H}_{\text{sop,r}} & \mathbf{H}_{\text{sop}} \end{bmatrix}, \quad \mathbf{H}_{\text{sv,r}} \triangleq \text{diag}\left[{}^{1}\mathbf{H}_{\text{sv,r}}, \ldots, {}^{N}\mathbf{H}_{\text{sv,r}}\right]$$

$${}^{n}\mathbf{H}_{\text{sv},r} = \begin{bmatrix} \mathbf{0}_{1\times 3} & {}^{n}\hat{\mathbf{l}}_{\text{sv},1}^{\mathsf{T}} & \mathbf{0}_{1\times 9} & \boldsymbol{h}_{\text{clk}}^{\mathsf{T}} \\ \vdots & \vdots & \vdots & \vdots \\ \mathbf{0}_{1\times 3} & {}^{n}\hat{\mathbf{l}}_{\text{sv},L}^{\mathsf{T}} & \mathbf{0}_{1\times 9} & \boldsymbol{h}_{\text{clk}}^{\mathsf{T}} \end{bmatrix}$$

$$\mathbf{H}_{\text{sop,r}} \triangleq \text{diag}\left[{}^{1}\mathbf{H}_{\text{sop,r}}, \ldots, {}^{N}\mathbf{H}_{\text{sop,r}}\right]$$

where ${}^{n}\mathbf{H}_{\text{sop,r}}$ has the same structure as ${}^{n}\mathbf{H}_{\text{sv,r}}$, except ${}^{n}\hat{\mathbf{l}}_{\text{sv},l}^{\mathsf{T}}$ is replaced with ${}^{n}\hat{\mathbf{l}}_{\text{sop},m}^{\mathsf{T}}$

$$\mathbf{H}_{\text{sop}} \triangleq \left[{}^{1}\mathbf{H}_{\text{sop}}^{\mathsf{T}}, \ldots, {}^{N}\mathbf{H}_{\text{sop}}^{\mathsf{T}}\right]^{\mathsf{T}}$$

$${}^{n}\mathbf{H}_{\text{sop}} = \text{diag}\left[{}^{n}\mathbf{H}_{\text{sop},1}, \ldots, {}^{n}\mathbf{H}_{\text{sop},M}\right]$$

$${}^{n}\hat{\mathbf{l}}_{\text{sv},l} \triangleq \frac{\hat{\boldsymbol{r}}_{b_n} - \boldsymbol{r}_{\text{sv},l}}{\|\hat{\boldsymbol{r}}_{b_n} - \boldsymbol{r}_{\text{sv},l}\|}, \quad {}^{n}\hat{\mathbf{l}}_{\text{sop},m} \triangleq \frac{\hat{\boldsymbol{r}}_{b_n} - \hat{\boldsymbol{r}}_{\text{sop},m}}{\|\hat{\boldsymbol{r}}_{b_n} - \hat{\boldsymbol{r}}_{\text{sop},m}\|}$$

$${}^{n}\mathbf{H}_{\text{sop},m} \triangleq \left[-{}^{n}\hat{\mathbf{l}}_{\text{sop},m}^{\mathsf{T}},\, -\boldsymbol{h}_{\text{clk}}^{\mathsf{T}}\right], \quad \boldsymbol{h}_{\text{clk}} \triangleq [1,\, 0]^{\mathsf{T}}$$

and $\mathbf{R}$ is the measurement noise covariance. Note that $\mathbf{R}$ is not necessarily diagonal, since there are no assumptions made on the measurement noise statistics, except that $\mathbf{R} \succ \mathbf{0}$.

Note that if GNSS pseudoranges become completely unavailable, i.e., $L = 0$ and $z \equiv z_{\text{sop}}$, the state and covariance corrections are identical, except that the Jacobian is adjusted to account for GNSS SV pseudoranges no longer being available, specifically

$$\mathbf{H} \equiv \left[\mathbf{H}_{\text{sop},r},\, \mathbf{H}_{\text{sop}}\right]. \tag{20}$$

V. EVENT-BASED COMMUNICATION STRATEGY

This section develops an event-based communication strategy, which aims to minimize the amount of communicated data between collaborators, subject to a specified constraint on the vehicles' position estimation errors.

A. Problem Formulation

1) *Objective:* The objective of the event-based information fusion scheme is to minimize the rate at which the data packets $\{\boldsymbol{\Lambda}_n\}_{n=1}^{N}$ are broadcasted by the navigating vehicles, while maintaining a specified estimation performance constraint. The performance constraint is defined such that the norm of any vehicle's position estimation error $\tilde{\boldsymbol{r}}_{b_n}$ remains below a specified maximum threshold $\xi_{\max}$ with probability p. Systems designers may be interested in the overall magnitude of the error (2-norm) or the maximum error in a coordinate direction (∞-norm). To this end, two norms are considered: $\|\tilde{\boldsymbol{r}}_{b_n}\|_2$ and $\|\tilde{\boldsymbol{r}}_{b_n}\|_\infty$. Formally, the performance constraint to be maintained is

$$\Pr\left[\|\tilde{\boldsymbol{r}}_{b_n}\|_q \le \xi_{\max}\right] \ge p, \quad n = 1, \ldots, N \tag{21}$$

where $\Pr[A]$ denotes the probability of event A and q is user-specified to be $q \equiv 2$ or $q \equiv \infty$.

2) *Approach:* In contrast to all vehicles transmitting $\{\boldsymbol{\Lambda}_n\}_{n=1}^{N}$ at a fixed rate, which is the rate at which measurements are made; in the event-based scheme, $\{\boldsymbol{\Lambda}_n\}_{n=1}^{N}$ are transmitted and an EKF measurement update is performed only if (21) would be violated, if transmission of $\{\boldsymbol{\Lambda}_n\}_{n=1}^{N}$ does not occur. Since the position estimation error $\tilde{\boldsymbol{r}}_{b_n}$ *is not* available to the navigating vehicles, an online test is formulated using each vehicle's position estimation error covariance $\mathbf{P}_{\boldsymbol{r}_{b_n}}$, which *is* available to each vehicle via the EKF estimator. This online test will be used to check if (21) would be violated if transmission does not occur. In the next two sections, two tests are formulated: $\|\tilde{\boldsymbol{r}}_{b_n}\|_2$ and $\|\tilde{\boldsymbol{r}}_{b_n}\|_\infty$. Note that SOP measurements are discarded unless an event is triggered to maintain state estimation consensus among the filters running at each vehicle. If the navigation filter designer wishes, local EKF measurements may be processed between event triggers, and then a covariance intersection may be performed after an event is triggered [34]. In what follows, the true estimation error covariance is approximated using the one estimated by the EKF. This approximation is reasonable when positioning errors are small, which yield small linearization errors. The position errors are small initially, since the vehicles initially have access to GPS, and then small errors are maintained after GPS is cut off by correcting the INS using the SOPs.

B. Two-Norm Test Formulation

LEMMA V.1 Consider the performance constraint (21) with $q \equiv 2$ and a user specified p and $\xi_{\max}$. Testing if (21) is violated is equivalent to checking if

$$\|\mathbf{P}_{\boldsymbol{r}_{b_n}}\|_2 \le \frac{\xi_{\max}^2}{\eta_n}, \quad n = 1, \ldots, N \tag{22}$$

is violated, where $\mathbf{P}_{\boldsymbol{r}_{b_n}}$ is the estimation error covariance associated with the nth navigating vehicle, and η_n is the value of the inverse cumulative distribution function (CDF) of the Mahalanobis norm-squared of the estimation error $\|\tilde{\boldsymbol{r}}_{b_n}\|_{\mathrm{M}}^2$ evaluated at p.

PROOF To formulate the test for (21) corresponding to $\|\tilde{\boldsymbol{r}}_{b_n}\|_2$, the Mahalanobis norm (or Mahalanobis distance) of the position estimation error for vehicle n, denoted $\|\tilde{\boldsymbol{r}}_{b_n}\|_{\mathrm{M}}$, is used, which is given by

$$\|\tilde{\boldsymbol{r}}_{b_n}\|_{\mathrm{M}}(k) = \sqrt{[\boldsymbol{r}_{b_n}(k) - \hat{\boldsymbol{r}}_{b_n}(k|k)]^{\mathsf{T}} \mathbf{P}_{\boldsymbol{r}_{b_n}}^{-1}(k|k)[\boldsymbol{r}_{b_n}(k) - \hat{\boldsymbol{r}}_{b_n}(k|k)]}. \quad (23)$$

In this context, the Mahalanobis norm provides a measure of how many standard deviations the true position is away from the estimated position. In what follows, it will be shown how $\|\tilde{\boldsymbol{r}}_{b_n}\|_{\mathrm{M}}$ is related to the performance constraint (21), and how it leads to a simple test that each vehicle may perform to determine if $\{\boldsymbol{\Lambda}_n\}_{n=1}^N$ should be transmitted. Time dependency will be dropped in the sequel to simplify the notation.

Since the covariance $\mathbf{P}_{\boldsymbol{r}_{b_n}}$ is a real-valued, symmetric, positive-definite matrix, it has an eigendecomposition

$$\mathbf{P}_{\boldsymbol{r}_{b_n}} = \mathbf{U}_n \mathbf{D}_n \mathbf{U}_n^{\mathsf{T}}$$
$$\mathbf{D} = \operatorname{diag}\left[\lambda_{n,1}, \lambda_{n,2}, \lambda_{n,3}\right] \quad (24)$$

where $\lambda_{n,i}$ is the ith eigenvalue of $\mathbf{P}_{\boldsymbol{r}_{b_n}}$ and $\mathbf{U}_n$ is an orthogonal matrix whose ith column is the ith eigenvector of $\mathbf{P}_{\boldsymbol{r}_{b_n}}$. Substituting (24) into (23) and squaring both sides yields

$$\|\tilde{\boldsymbol{r}}_{b_n}\|_{\mathrm{M}}^2 = \boldsymbol{\xi}_n^{\mathsf{T}} \mathbf{D}_n^{-1} \boldsymbol{\xi}_n \quad (25)$$
$$\boldsymbol{\xi}_n \triangleq \mathbf{U}^{\mathsf{T}}(\boldsymbol{r}_{b_n} - \hat{\boldsymbol{r}}_{b_n}). \quad (26)$$

The vector $\boldsymbol{\xi}_n = [\xi_{n,1}, \xi_{n,2}, \xi_{n,3}]^{\mathsf{T}}$ is the position estimation error $\tilde{\boldsymbol{r}}_{b_n}$ expressed in frame $\{g\}$, rotated by the orthogonal (rotation) matrix $\mathbf{U}^{\mathsf{T}}$ into a coordinate frame $\{f\}$, whose axes coincide with the principal axes of an ellipsoid. This ellipsoid is known as the probability concentration ellipsoid $\mathcal{E}$, which represents the probability p of the error $\boldsymbol{\xi}_n$ lying on or within the ellipsoid [59], where

$$p = \Pr\left[\|\tilde{\boldsymbol{r}}_{b_n}\|_{\mathrm{M}}^2 \leq \eta_n\right]. \quad (27)$$

Given p and the distribution of $\|\tilde{\boldsymbol{r}}_{b_n}\|_{\mathrm{M}}^2$, the value η_n can be determined [60]. The principal axes of the confidence ellipsoid $\mathcal{E}$ are found by expanding the righthand side of (25) and substituting the expansion into the inequality $\|\tilde{\boldsymbol{r}}_{b_n}\|_{\mathrm{M}}^2 \leq \eta_n$ from (27), which gives

$$\frac{\xi_{n,1}^2}{\eta_n \lambda_{n,1}} + \frac{\xi_{n,2}^2}{\eta_n \lambda_{n,2}} + \frac{\xi_{n,3}^2}{\eta_n \lambda_{n,3}} \leq 1 \quad (28)$$

which is the equation of an ellipsoid with radii $\sqrt{\eta_n \lambda_{n,i}}$, for $i = 1, 2, 3$. The ellipsoid and the bounding constraint corresponding to $\|\tilde{\boldsymbol{r}}_{b_n}\|_2 \leq \xi_{\max}$ are illustrated as a 2-D example in Fig. 3.

Note that, although the value of $\boldsymbol{\xi}_n$ *is not available* to the navigating vehicle, the eigenvalues $\{\lambda_{n,i}\}_{i=1}^3$ and the specified probability p governing the size and shape of the ellipsoid $\mathcal{E}$ *are available* and upper-bound the "size" of $\boldsymbol{\xi}_n$. Specifically, $\|\boldsymbol{\xi}_n\|_2$ is bounded by the major axis of $\mathcal{E}$, which is given by

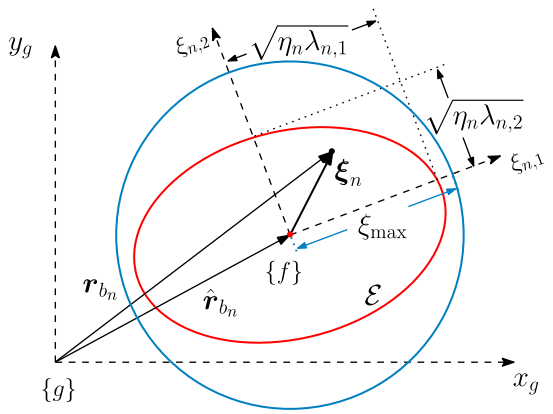

Fig. 3. Probability concentration ellipse $\mathcal{E}$ with origin $\hat{\boldsymbol{r}}_{b_n}$ and radii $\sqrt{\eta_n \lambda_{n,i}}$, $i = 1, 2$.

$$\max_{\mathcal{E}} \|\boldsymbol{\xi}_n\|_2 = \max_{\mathcal{E}} \|\tilde{\boldsymbol{r}}_{b_n}\|_2 = \sqrt{\eta_n \lambda_{\max}[\mathbf{P}_{\boldsymbol{r}_{b_n}}]} \quad (29)$$

where $\max_{\mathcal{E}} d$ denotes the maximum value of d in set $\mathcal{E}$, $\lambda_{\max}[\mathbf{X}]$ denotes the maximum eigenvalue of $\mathbf{X}$, and $\|\tilde{\boldsymbol{r}}_{b_n}\|_2 = \|\boldsymbol{\xi}\|_2$ has been used, which holds since the 2-norm is invariant under coordinate frame rotation. Since the error constraint $\xi_{\max}$ is also invariant under coordinate frame rotation, the problem boils down to checking if the major axis of the ellipsoid $\mathcal{E}$ is less than $\xi_{\max}$, i.e.,

$$\sqrt{\eta_n \lambda_{\max}[\mathbf{P}_{\boldsymbol{r}_{b_n}}]} \leq \xi_{\max}. \quad (30)$$

Finally, noting that $\lambda_{\max}[\mathbf{P}_{\boldsymbol{r}_{b_n}}] = \|\mathbf{P}_{\boldsymbol{r}_{b_n}}\|_2$ for covariance matrices and by solving (30) in terms of the specified constraints, the test simplifies to checking the violation of

$$\|\mathbf{P}_{\boldsymbol{r}_{b_n}}\|_2 \leq \frac{\xi_{\max}^2}{\eta_n}.$$

■

C. Infinity-Norm Test Formulation

LEMMA V.2 Consider the performance constraint (21) with $q \equiv \infty$ and a user-specified coordinate frame $\{\mathrm{g}\}$, probability p, and maximum error $\xi_{\max}$. Testing if (21) is violated is equivalent to checking if

$$\|\mathbf{P}_{\boldsymbol{r}_{b_n}}\|_{\max} \leq \frac{\xi_{\max}^2}{\eta_n}, \quad n = 1, \ldots, N \quad (31)$$

is violated, where $\|\mathbf{X}\|_{\max}$ denotes the maximum norm of a matrix $\mathbf{X} \in \mathbb{R}^{d_1 \times d_2}$, which is given by

$$\|\mathbf{X}\|_{\max} \triangleq \max\{|\mathbf{X}_{ij}| \,|i = 1, \ldots, d_1,\ j = 1, \ldots, d_2\}.$$

The matrix $\mathbf{P}_{\boldsymbol{r}_{b_n}}$ is the position estimation error covariance associated with the nth navigating vehicle and η_n is the value of the inverse cdf of the Mahalanobis norm-squared of the estimation error $\|\tilde{\boldsymbol{r}}_{b_n}\|_{\mathrm{M}}^2$ evaluated at p.

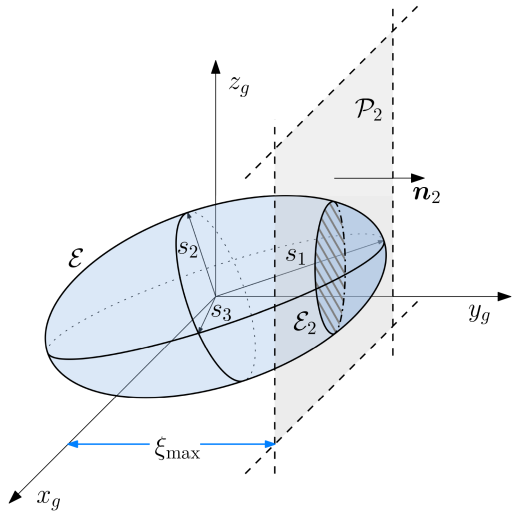

Fig. 4. Probability concentration ellipsoid $\mathcal{E}$ with radii $s_\alpha \triangleq \sqrt{\eta_n \lambda_{n,\alpha}}$, $\alpha = 1, 2, 3$, and plane $\mathcal{P}_2$, representing one of six surfaces of the cube constraint. If $\mathcal{E}$ intersects the cube constraint at plane $\mathcal{P}_2$, then the ellipse $\mathcal{E}_2$ exists.

PROOF The test formulation and the ∞-norm error constraint are coordinate frame dependent, since the ∞-norm is *not* invariant under coordinate frame rotations. Therefore, the coordinate frame $\{g\}$ in which the test is conducted is specified by the user along with $\xi_{\max}$ and p, (e.g., test if p is less than the probability that the maximum of the north, east, and down (NED) errors is less than $\xi_{\max}$). In contrast to the bounding circle (sphere in 3-D) associated with the constraint $\|\tilde{\boldsymbol{r}}_{b_n}\|_2 \leq \xi_{\max}$ in Fig. 3, the constraint $\|\tilde{\boldsymbol{r}}_{b_n}\|_\infty \leq \xi_{\max}$ is geometrically interpreted as a square (cube in 3-D), which is symmetric about the origin, with each of its sides a distance of $\xi_{\max}$ from the origin. Since the probability concentration ellipsoid $\mathcal{E}$ provides a bounding surface for which the estimation error is contained within, for a specified probability p, a test will be formulated to check if $\mathcal{E}$ is contained within the cube corresponding to $\|\tilde{\boldsymbol{r}}_{b_n}\|_\infty \leq \xi_{\max}$.

The ellipsoid $\mathcal{E}$ expressed in $\{g\}$ is found by substituting (23) into the inequality $\|\tilde{\boldsymbol{r}}_{b_n}\|_{\mathrm{M}}^2 \leq \eta_n$ from (27), which gives

$$\frac{1}{\eta_n}\tilde{\boldsymbol{r}}_{b_n}^{\mathsf{T}}\mathbf{P}_{\tilde{\boldsymbol{r}}_{b_n}}^{-1}\tilde{\boldsymbol{r}}_{b_n} \leq 1. \tag{32}$$

The bounding cube is represented as a collection of six planes, defined by normal vectors $\pm\boldsymbol{n}_i$, $i = 1, 2, 3$, each of which is parallel to the corresponding unit vectors that define the coordinate frame $\{g\}$, e.g., $\boldsymbol{n}_2$ corresponds to the y_g direction and is parallel to $\boldsymbol{e}_2$, where $\boldsymbol{e}_i \in \mathbb{R}^3$ is the standard unit basis vector, containing a one in the ith position and zeros elsewhere. Given the constraint $\xi_{\max}$, the ith plane, denoted $\mathcal{P}_i$, is given by

$$\boldsymbol{n}_i^{\mathsf{T}}\tilde{\boldsymbol{r}}_{b_n} - \xi_{\max} = 0. \tag{33}$$

If the ellipsoid $\mathcal{E}$ extends beyond the plane $\mathcal{P}_i$, an intersecting ellipse $\mathcal{E}_i \triangleq \mathcal{E} \cap \mathcal{P}_\alpha$ will exist. The relationship between $\mathcal{E}$, $\mathcal{P}_i$, and $\mathcal{E}_i$ for $i = 2$ are illustrated in Fig. 4.

Since $\mathcal{E}$ and the bounding cube are both symmetric about the origin of $\{g\}$, it suffices to test if $\exists\mathcal{E}_i$, for only the three positive directions to determine if $\mathcal{E}$ is contained within the bounding cube. In what follows, the test for a general ith plane is formulated. The points on and within the intersecting ellipse $\mathcal{E}_i$ represents the solution space that satisfies both (32) and (33). The expression for this solution space is found using the next steps. First, the ith parallel vectors are set equal to each other, i.e., $\boldsymbol{n}_i \equiv \boldsymbol{e}_i$, which gives

$$\boldsymbol{e}_i^{\mathsf{T}}\tilde{\boldsymbol{r}}_{b_n} = \xi_{\max} \tag{34}$$

which equates the ith element of $\tilde{\boldsymbol{r}}_{b_n}$ to $\xi_{\max}$. Second, (34) is substituted into (32). For convenience, in the remainder of the test formulation, $\tilde{\boldsymbol{r}}_{b_n}$ will be arranged to place $\xi_{\max}$ to the first element of a vector and the remaining elements will follow in a newly defined vector $\boldsymbol{u}_i \in \mathbb{R}^2$. The matrix $\mathbf{P}_{\tilde{\boldsymbol{r}}_{b_n}}^{-1}$ is modified accordingly, so that the ith diagonal element is placed into the top-left element, denoted β_i and the corresponding cross-correlation elements are permutated into vector $\boldsymbol{b}_i \in \mathbb{R}^2$, and the remaining elements are placed into $\mathbf{A} \in \mathbb{R}^{2\times 2}$. These permutations are performed using a permutation matrix $\mathbf{N}_i$ through

$$\boldsymbol{y}_i \triangleq \mathbf{N}_i\tilde{\boldsymbol{r}}_{b_n} = \begin{bmatrix}\xi_{\max}\\ \boldsymbol{u}_i\end{bmatrix}, \quad \mathbf{Y}_i \triangleq \mathbf{N}_i\mathbf{P}_{\tilde{\boldsymbol{r}}_{b_n}}^{-1}\mathbf{N}_i^{\mathsf{T}} = \begin{bmatrix}\beta_i & \boldsymbol{b}_i^{\mathsf{T}}\\ \boldsymbol{b}_i & \mathbf{A}_i\end{bmatrix}$$

$$\mathbf{N}_i \triangleq \begin{bmatrix}\boldsymbol{e}_i^{\mathsf{T}}\\ \mathbf{G}_i\end{bmatrix}, \quad \mathbf{G}_i = \begin{bmatrix}\boldsymbol{e}_{\alpha\setminus i}^{\mathsf{T}}\\ \boldsymbol{e}_{\alpha+1\setminus i}^{\mathsf{T}}\end{bmatrix}, \quad \alpha = 1, 2, 3.$$

Noting the properties of permutation matrices

$$\mathbf{N}_i\mathbf{N}_i^{\mathsf{T}} = \mathbf{N}_i^{\mathsf{T}}\mathbf{N}_i = \mathbf{I}_{3\times 3}$$

the ellipsoid equation in (32) may be rewritten as

$$\boldsymbol{y}_i^{\mathsf{T}}\mathbf{Y}_i\boldsymbol{y}_i = \begin{bmatrix}\xi_{\max}\\ \boldsymbol{u}_i\end{bmatrix}^{\mathsf{T}}\begin{bmatrix}\beta_i & \boldsymbol{b}_i^{\mathsf{T}}\\ \boldsymbol{b}_i & \mathbf{A}_i\end{bmatrix}\begin{bmatrix}\xi_{\max}\\ \boldsymbol{u}_i\end{bmatrix} \leq \eta_n. \tag{35}$$

To check if there is a feasible solution to (35), the lefthand side of the inequality is minimized over the remaining variables $\boldsymbol{u}_i$ and then the optimal value is compared with the righthand side of the inequality. Since $\mathbf{P}_{\tilde{\boldsymbol{r}}_{b_n}}^{-1} \succ \mathbf{0}$, then $\mathbf{A} = \mathbf{G}_\alpha\mathbf{P}_{\tilde{\boldsymbol{r}}_{b_n}}^{-1}\mathbf{G}^{\mathsf{T}} \succ \mathbf{0}$, making this a convex optimization problem with a known optimal value, which is given by [61]

$$\inf_{\boldsymbol{u}}\begin{bmatrix}\xi_{\max}\\ \boldsymbol{u}_i\end{bmatrix}^{\mathsf{T}}\begin{bmatrix}\beta_i & \boldsymbol{b}_i^{\mathsf{T}}\\ \boldsymbol{b}_i & \mathbf{A}_i\end{bmatrix}\begin{bmatrix}\xi_{\max}\\ \boldsymbol{u}_i\end{bmatrix} = \xi_{\max}^2\mathbf{S}_i \tag{36}$$

where $\mathbf{S}_i$ is the Schur complement of $\mathbf{A}_i$, which is equal to

$$\mathbf{S}_i = \beta_i - \boldsymbol{b}_i^{\mathsf{T}}\mathbf{A}_i^{-1}\boldsymbol{b}_i. \tag{37}$$

Checking if $\exists\mathcal{E}_i$ for $i = 1, 2, 3$ to determine if $\mathcal{E}$ is intersecting the bounding cube is equivalent to checking if $\mathbf{S}_i^{-1} \geq \xi_{\max}^2/\eta_n$. Conversely, checking if $\nexists\mathcal{E}_i$ for $i = 1, 2, 3$ to determine if $\mathcal{E}$ is contained within the bounding cube is equivalent to checking if

$$\mathbf{S}_i^{-1} < \frac{\xi_{\max}^2}{\eta_n} \quad \text{for} \quad i = 1, 2, 3. \tag{38}$$

Note that the Schur complement $\mathbf{S}_i$ is nonsingular, since $\mathbf{P}_{\boldsymbol{r}_{b_n}}^{-1} \succ \mathbf{0}$ [61].

The number of tests in (38) can be reduced from three to one by testing only $\max_i \mathbf{S}_i^{-1}$. Conveniently, this value is equal to the maximum entry of $\mathbf{P}_{\boldsymbol{r}_{b_n}}$. To see this, consider the matrix block inversion property of the Schur complement [61]

$$\begin{bmatrix} \beta_i & \boldsymbol{b}_i^{\mathrm{T}} \\ \boldsymbol{b}_i & \mathbf{A}_i \end{bmatrix}^{-1} = \begin{bmatrix} \mathbf{S}_i^{-1} & -\mathbf{S}_i^{-1}\boldsymbol{b}_i^{\mathrm{T}}\mathbf{A}_i^{-1} \\ -\mathbf{A}_i^{-1}\mathbf{b}_i\mathbf{S}_i^{-1} & \mathbf{A}_i^{-1}+\mathbf{A}_i^{-1}\boldsymbol{b}_i\mathbf{S}_i^{-1}\boldsymbol{b}_i^{\mathrm{T}}\mathbf{A}_i^{-1} \end{bmatrix} \tag{39}$$

The lefthand side of (39) is

$$\mathbf{Y}_i^{-1} = \mathbf{N}_i \mathbf{P}_{\tilde{\boldsymbol{r}}_{b_n}} \mathbf{N}_i^{\mathrm{T}}. \tag{40}$$

From (39), one can deduce that $\mathbf{S}_i^{-1}$ is equal to the top-left element of $\mathbf{Y}_i^{-1}$. From (40), one can conclude that the top-left element of $\mathbf{Y}_i^{-1}$ is equal to the ith diagonal element of $\mathbf{P}_{\tilde{\boldsymbol{r}}_{b_n}}$, since permutations conducted on the inverse of a matrix correspond to permutations conducted on the matrix itself. Finally, since the largest elements of a symmetric positive-definite matrix are the diagonal elements, it suffices to check the largest element of the matrix. Therefore, the test to determine if the performance constraint (21) with $q \equiv \infty$ will be violated, boils down to each vehicle checking

$$\|\mathbf{P}_{\boldsymbol{r}_{b_n}}\|_{\max} \leq \frac{\xi_{\max}^2}{\eta_n}.$$

■

If the test (22) or (31) fails for any vehicle, the vehicle whose test fails requests all vehicles to transmit their $\{\mathbf{\Lambda}_n\}_{n=1}^N$, and subsequently all vehicles perform an EKF correction upon receiving the communicated packets from other vehicles. An event-trigger threshold on the EKF-produced 3σ error standard deviations of the vehicles' position states, over which the transmission of $\{\mathbf{\Lambda}_n\}_{n=1}^N$ is requested, can be found by taking the square root of (22), which yields

$$3\sigma \leq 3\frac{\xi_{\max}}{\sqrt{\eta_n}}. \tag{41}$$

VI. SIMULATIONS

This section presents simulation results demonstrating the event-based information transmission schemes developed in Section V. First, the simulation environment and settings are discussed. Then, the probability density function (pdf) of $\|\tilde{\boldsymbol{r}}_{b_n}\|_{\mathrm{M}}^2$ is characterized, which is needed to compute η_n using the inverse cdf on (27).

A. Simulation Environment and Settings

The simulation environment consists of $N = 4$ UAV-mounted receivers and $M = 6$ SOP transmitters. The receivers were set to have GPS available for the first 50 s of their trajectory and then unavailable for the remaining 150 s portion of the trajectory. SOP pseudoranges were available for their entire trajectories. The simulated UAV trajectories, SOP transmitters' positions, and the UAVs' positions at the time GPS was set to become unavailable are illustrated in Fig. 5. The following describes the methods used to produce the simulated data.

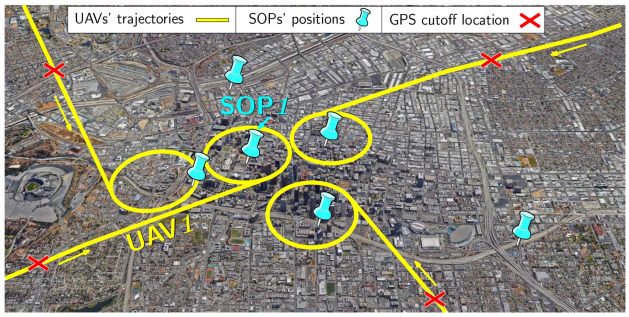

Fig. 5. True trajectories the UAVs traversed (yellow), SOP transmitters' positions (blue pins), and the UAVs' positions at the time GPS was cut off (red).

1) *UAVs' Trajectories:* The UAVs' simulated trajectories were generated using a standard six degree of freedom (6DoF) kinematic model for airplanes [57]. Each vehicle performed the same maneuvers, which included the following segments conducted in succession over a 200 s period: 10 s straight and level linear acceleration along the direction of travel; 5 ° pitching climb for 30 s; 22 s straight and level linear velocity, while rolling to 60°; five 60 ° left-banking turns. These trajectory segments were chosen because they collectively excite all 6DoF of the UAVs, i.e., both horizontal and vertical directions and all three angles (roll, pitch, and yaw), allowing the event-based communication strategies to be studied under various maneuvers.

2) *IMU Data:* The gyroscope and accelerometer data were generated at 100 Hz using the simulated vehicles' accelerations and rotation rates through (4) and (5), respectively. The evolution of each vehicle's gyroscope and accelerometer biases was generated according to (6) and (7), respectively, using driving process noise with spectra $\mathbf{S}_{\boldsymbol{w}_{\mathrm{gyr}},n} \equiv (10^{-8}) \cdot \mathbf{I}_{3\times 3}$ and $\mathbf{S}_{\boldsymbol{w}_{\mathrm{acc}},n} \equiv 10^{-8} \cdot \mathbf{I}_{3\times 3}$, respectively. The power of the corrupting white noise was set to correspond to a consumer-grade IMU. IMUs of this quality typically state the noise values in terms of accumulated noise. Each axis of the IMU was set to have an accumulated noise of 0.3 deg /s and 2.5 milligravities for the gyroscope and accelerometer, respectively. These spectra are mapped to the discrete-time noise covariances $\mathbf{Q}_{\boldsymbol{n}_{\mathrm{gyr}},n}$, $\mathbf{Q}_{\boldsymbol{n}_{\mathrm{acc}},n}$, $\mathbf{Q}_{\boldsymbol{w}_{\mathrm{gyr}},n}$, and $\mathbf{Q}_{\boldsymbol{w}_{\mathrm{acc}},n}$ through the equations provided in Appendix A.

3) *Receiver Clock:* Each UAV-mounted receiver was set to be equipped with a typical temperature-compensated crystal oscillator (TCXO), with parameters $\{h_{0,r_n}, h_{-2,r_n}\}_{n=1}^4 = \{9.4 \times 10^{-20}, 3.8 \times 10^{-21}\}$. These parameters are used to compute the process noise covariance $\mathbf{Q}_{\mathrm{clk,r},n}$ that drive the receiver clock dynamics found according to (1).

4) *GPS Pseudoranges:* GPS L1 C/A pseudoranges were generated at 1 Hz according to (10). The position of each GPS satellite was generated by producing their orbits using Receiver Independent Exchange (RINEX) files,

downloaded from a continuously operating reference station (CORS) server [62]. Pseudorange from 11 GPS satellites ($L = 11$) were set to be available for $t \in [0, 50)$ s, and unavailable ($L = 0$) for $t \in [50, 200]$ s. The GPS pseudorange measurement noise terms were set to be independent from each other with measurement noise variance computed according to [63]

$$ {}^{n}\sigma^2_{\text{sv},l,j} = \frac{c^2 t_{\text{eml}} B_{\text{DLL}} T_c^2 \sigma_s^2}{2^{n}(C/N_0)_{l,j}} \left[1 + \frac{1}{T_{\text{CO}}\, {}^{n}(C/N_0)_{l,j}} \right] \tag{42} $$

where $t_{\text{eml}} \equiv 0.5$ chips is the early minus-late correlator spacing, $B_{\text{DLL}} \equiv 0.05$ Hz is the delay lock loop (DLL) bandwidth, $T_c \equiv 1/(1.023 \times 10^6)$ s is the chip duration, ${}^{n}(C/N_0)_{l,j}$ (in Hz) is the time-varying received carrier-to-noise ratio at UAV n from satellite l, which was derived from the RINEX files, $\sigma_s \equiv 17$ is a scaling parameter to account for unmodeled errors, and $T_{\text{CO}} \equiv 10$ ms is the coherent integration time. Equation (42) is the model used in this work; however, other models may be used. Another common model often employed is the scaled C/N_0 - elevation model [64]. The point at which GPS was cut off is illustrated as a red "X" in Fig. 5.

5) *SOP Pseudoranges:* Pseudoranges were generated to the SOPs at 5 Hz according to (9). The evolution of each SOP's clock bias was modeled according to the dynamics discussed in Section III-A, using parameters that correspond to a typical oven-controlled crystal oscillator (OCXO), with $\{h_{0,\text{sop},m}, h_{-2,\text{sop},m}\}_{m=1}^{6} = \{8 \times 10^{-20}, 4 \times 10^{-23}\}$. The SOP transmitters' positions $\{\boldsymbol{r}_{\text{sop},m}\}_{m=1}^{6}$ were surveyed from cellular tower locations in downtown Los Angeles, California, USA. The SOP pseudorange measurement noise terms were set to be independent with a measurement noise variance according to (42), except that $t_{\text{eml}} \equiv 1$, ${}^{n}\sigma^2_{\text{sv},l,j}$ is replaced with ${}^{n}\sigma^2_{\text{sop},m,j}$, $T_c \equiv 1/(1.2288 \times 10^6)$, $\sigma_s \equiv 22$, $T_{CO} \equiv 1/37.5$ s, and the carrier-to-noise ratio ${}^{n}(C/N_0)_{m,j}$ is replaced with a time-varying log-distance path-loss model [65]

$$ {}^{n}(C/N_0)'_{m,j} = P_0 - 10\gamma \cdot \log_{10}(d(j)/D_0) $$
$$ {}^{n}(C/N_0)_{m,j} = 10^{\left[{}^{n}(C/N_0)'_{m,j}/10\right]} $$

where $P_0 \equiv 56$ dB-Hz is a calibration carrier-to-noise ratio at a distance $D_0 \equiv 1400$ m, $d(j) \triangleq \|{}^{e}\boldsymbol{r}_b(j) - {}^{e}\boldsymbol{r}_{\text{sop},m}\|_2$, and $\gamma \equiv 2$ is the path-loss exponent. The calibration values P_0 and D_0 are values commonly observed by the authors during experimental campaigns [12], [66], [67]. The SOP pseudorange measurement noise variance computation assumes that the correlation function within the DLL is equivalent to GPS. This is a reasonable assumption for cellular code division multiple access (CDMA) signals, when t_{eml} is between 0.8 and 1.25 chips. More sophisticated models for cellular CDMA are discussed in [68], for long-term evolution (LTE) are discussed in [69], and for 5 G are discussed in [70].

B. EKF-Based CIRSLAM Filter Initialization

The initial estimates (at $t = 0$ s) of the UAVs' states were initialized by drawing a random error vector from a multivariate Gaussian distribution and then adding the error to the "ground truth" state at $t = 0$. This initialization method is used instead of directly drawing the state estimate to deal with the quaternion initialization, which requires special handling. This method is described in the next three steps. First, the random error for each UAV was drawn according to

$$ \tilde{\boldsymbol{x}}_{\text{r},n}(0|0) \sim \mathcal{N}\left[\boldsymbol{0}_{17\times 1},\ \mathbf{P}_{\boldsymbol{x}_{\text{r},n}}(0|0)\right] $$
$$ \mathbf{P}_{\boldsymbol{x}_{\text{r}},n}(0|0) \triangleq \text{diag}\left[\mathbf{P}_{\boldsymbol{x}_{\text{ins}},n}(0|0),\ \mathbf{P}_{\boldsymbol{x}_{\text{clk,r}}}(0|0)\right] $$
$$ \mathbf{P}_{\boldsymbol{x}_{\text{ins}},n}(0|0) \equiv \text{diag}\left[\left(10^{-2}\right)\cdot\mathbf{I}_{3\times 3},\ 9\cdot\mathbf{I}_{3\times 3},\ \mathbf{I}_{3\times 3},\ \left(10^{-4}\right)\cdot\mathbf{I}_{6\times 6}\right] $$
$$ \mathbf{P}_{\boldsymbol{x}_{\text{clk,r},n}}(0|0) \equiv \text{diag}\,[9,\ 1] $$

were $\boldsymbol{a} \sim \mathcal{N}(\boldsymbol{\mu}, \mathbf{C})$ indicates that $\boldsymbol{a}$ is Gaussian-distributed with mean $\boldsymbol{\mu}$ and covariance $\mathbf{C}$. Second, to produce the initial quaternion estimate, two approaches are common and may be used. The small angle errors may be used to create a rotation matrix, which can then be converted to quaternion and multiplied by the true angle in order to produce a new quaternion, which will serve as the initial estimate. Alternatively, the resulting angle error $\boldsymbol{\theta} \in \mathbb{R}^3$, which are the first three elements of $\tilde{\boldsymbol{x}}_{\text{r},n}$, may be mapped to an error quaternion $\tilde{\boldsymbol{q}}_n \in \mathbb{R}^4$, which are then applied to the true state according to the equations discussed in [27, Appendix C]. Third, to produce initial estimates of the remaining states, the remaining error components of $\tilde{\boldsymbol{x}}_{\text{r},n}$ are applied to the true states as standard additive error.

The SOPs' state estimates were initialized according to $\hat{\boldsymbol{x}}_{\text{sop},m}(0|0) \sim \mathcal{N}[\boldsymbol{x}_{\text{sop},m}(0), \mathbf{P}_{\text{sop}}(0|0)]$, for $m = 1, \ldots, M$, where $\boldsymbol{x}_{\text{sop},m}(0) \equiv [\boldsymbol{r}^{\text{T}}_{\text{sop},m},\ 10^4,\ 10]^{\text{T}}$, and $\mathbf{P}_{\text{sop}}(0|0) \equiv (10^4) \cdot \text{diag}[\mathbf{I}_{3\times 3}\, 0.1,\ 0.01]$. This initialization scheme is used in simulation to ensure consistent initial priors in the EKF. In practice, if the initial SOPs' states are completely unknown, then a random position for each SOP may be drawn in the vicinity of the UAVs with a large enough uncertainty to encompass all possible points that a signal could be received from. The clock states may be initialized to zero with a large uncertainty. As long as there are enough vehicle's or the vehicles are moving, the position and clock states of the SOPs are observable. Observability conditions are thoroughly analyzed in [29], [71], [72]. In [72], it was found that although individual clock biases were stochastically unobservable, the position estimates are estimable. In addition, a study with varying receiver-to-transmitter geometric configurations and clock qualities was conducted in [52].

C. Mahalanobis Norm-Squared Distribution Characterization

In this section, the pdf of $\|\tilde{\boldsymbol{r}}_{b_n}\|^2_{\text{M}}$ is characterized, which is needed to compute η_n using the inverse cdf on (27). If $\tilde{\boldsymbol{r}}_{b_n}$ is Gaussian distributed, then $\|\tilde{\boldsymbol{r}}_{b_n}\|^2_{\text{M}}$ would be Chi-squared distributed, with three DoF. However, no assumption is made on the distribution of $\tilde{\boldsymbol{r}}_{b_n}$ during GPS availability or GPS unavailability and is characterized during each period. To determine the pdf of $\|\tilde{\boldsymbol{r}}_{b_n}\|^2_{\text{M}}$, 5×10^4 Monte Carlo runs were conducted using the environment illustrated in Fig. 5. The same simulation settings described in Section VI-A

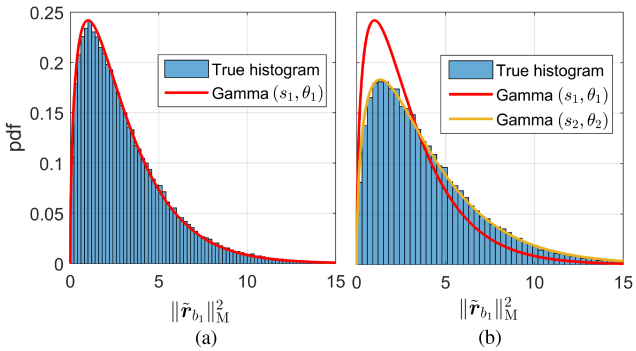

Fig. 6. (a) Histogram of $\|\tilde{\boldsymbol{r}}_{b_1}\|^2_{\mathrm{M}}$ during GPS availability ($L = 11$) and gamma distribution with parameters $s_1 = 3/2$ and $\theta_1 = 2$ and (b) histogram of $\|\tilde{\boldsymbol{r}}_{b_1}\|^2_{\mathrm{M}}$ during GPS unavailability ($L = 0$) and gamma distribution with parameters $s_2 = 3/2$ and $\theta_2 = 2.63$.

were used, except that each run used a different initial state estimate and different realizations of process and measurement noise. The value of $\|\tilde{\boldsymbol{r}}_{b_n}\|^2_{\mathrm{M}}$ was recorded for each run for $n = 1, \ldots, N$. GPS was set to be available for $t \in [0, 50)$ s with $L = 11$ and unavailable ($L = 0$) for $t \in [50, 200]$ s. Fig. 6 illustrates the Monte Carlo runs histogram of $\|\tilde{\boldsymbol{r}}_{b_n}\|^2_{\mathrm{M}}$ for UAV 1, from which it is deduced that the pdf follows a gamma distribution given by:

$$p\left(\|\tilde{\boldsymbol{r}}_{b_n}\|^2_{\mathrm{M}}; s, \theta\right) = \frac{1}{\Gamma(s)\theta^s}\left(\|\tilde{\boldsymbol{r}}_{b_n}\|^2_{\mathrm{M}}\right)^{s-1} e^{\frac{-\|\tilde{\boldsymbol{r}}_{b_n}\|^2_{\mathrm{M}}}{\theta}}$$

where s and θ are the shape and scale parameter of the gamma distribution, respectively, and Γ is the complete gamma function, which is defined as

$$\Gamma(z) \triangleq \int_0^\infty x^{z-1} e^{-x} dx.$$

A maximum likelihood estimator was employed to find the parameters s and θ [73]. During GPS availability ($L = 11$), the parameters were found to be $\{s, \theta\} \approx \{3/2, 2\}$, which is equivalent to a chi-squared distribution, with three DoF. During GPS unavailability ($L = 0$), the parameters were found to be $\{s, \theta\} \approx \{3/2, 2.63\}$. The estimated pdf for the GPS availability period is also plotted in Fig. 6(b) to show the shift in the pdf's scale parameter when GPS becomes unavailable.

It is important to note that during GPS unavailability the shape and scale parameters $\{s, \theta\}$ depend on the environment (e.g., number of SOPs and their geometric distribution). However, in a practical scenario, the parameters $\{s, \theta\}$ may be determined online when GPS is still available. To do this, the following procedure may be used. First, in addition to the EKF running that has access to GPS, a parallel EKF is run with GPS fictitiously cut off. Second, the estimated UAVs' positions using SOPs only (GPS unavailability) are difference with the GPS produced position estimates in order to calculate a time history of $\tilde{\boldsymbol{r}}_{b_n}$, $n = 1, \ldots, N$. Third, the time history $\tilde{\boldsymbol{r}}_{b_n}$ is downsampled to make it approximately white, since the errors are typically correlated for a short time. Fourth, the distribution of $\|\tilde{\boldsymbol{r}}_{b_n}\|^2_{\mathrm{M}}$ is characterized by passing the downsampled signal through a maximum likelihood to estimate the gamma distribution parameters [73].

D. Simulation Results

This section presents simulation results to demonstrate the event-based communication strategies to compare their resulting estimation performance and corresponding communication rates versus a fixed-rate communication scheme.

To this end, the same environment illustrated in Fig. 5 was simulated using the settings described in section VI-A. GPS was set to be available for $t \in [0, 50)$ s, and unavailable for $t \in [50, 200]$ s. Two EKF-CIRSLAM estimators were run to estimate the UAVs' trajectories. The only difference between the estimators is in when the communication of $\{\boldsymbol{\Lambda}_n\}_{n=1}^4$ takes place and the EKF correction step is performed: 1) fixed-rate, when measurements are made or 2) event-based, when any UAV violates (22) or (31).

Each estimator was initialized according to the procedure discussed in Section VI-B. For the event-based run, the two-norm ($q = 2$) test in (22) was employed, where the constraints specified on the UAVs' position estimates were set to be $\xi_{\max} \equiv 10$ m with a confidence probability $p \equiv 0.999$. Using this p and the shape and scale parameters found in Section VI-C, the inverse cdf of (27) evaluated to $\eta_1 \approx 16.27$ and $\eta_1 \approx 21.37$ for the GPS availability and unavailability periods, respectively. Plugging these values into (22) yielded $\|\mathbf{P}_{\boldsymbol{r}_{b_1}}(k|j)\|_2 \leq 6.15$ and $\|\mathbf{P}_{\boldsymbol{r}_{b_1}}(k|j)\|_2 \leq 4.68$ for the GPS available and unavailable periods, respectively. The infinity-norm ($q = \infty$) test in (31) was also employed on the UAVs' east, north, and down position covariance during a separate run. Plugging the above values into (31) yielded $\|\mathbf{P}_{\boldsymbol{r}_{b_1}}(k|j)\|_{\max} \leq 6.15$ and $\|\mathbf{P}_{\boldsymbol{r}_{b_1}}(k|j)\|_{\max} \leq 4.68$ for the GPS available and unavailable periods, respectively.

To visualize the reduction of the transmitted data, the accumulation of transmitted data was recorded for each scheme by summing the number of transmitted bits each time a packet transmission occurred. The size of the packet in bits was found by summing the number of values in (14) and setting each value to be a 32-bit float data type, as described in [58]. For a comparative analysis, the accumulation of transmitted data for transmitting raw IMU data was also recorded.

Fig. 7 shows the resulting east, north, and down errors and corresponding $\pm 3\sigma$ bounds of UAV 1 along with the $\pm 3\sigma$ bound event-trigger thresholds (41) during GPS unavailability. To avoid convoluting the plot, only results for the test in (22) are shown in Fig. 7, since it was found that the resulting EKF plots were very similar to using the infinity-norm ($q = \infty$) test in (31). This is due to the dominant *vertical* uncertainties, which make $\|\mathbf{P}_{\boldsymbol{r}_{b_1}}(k|j)\|_2 \|\mathbf{P}_{\boldsymbol{r}_{b_1}}(k|j)\|_{\max}$. Such uncertainty is due to the poor geometric diversity in the vertical direction for terrestrial SOPs. Fig. 8 shows the resulting $\log\{\det[\mathbf{P}_{\boldsymbol{r}_{b_1}}(k|j)]\}$ for using the fixed-rate and

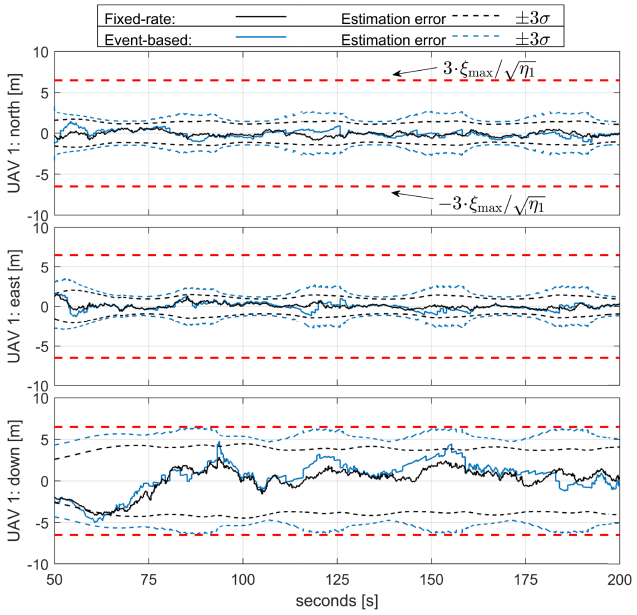

Fig. 7. Resulting north, east, and down errors and corresponding $\pm 3\sigma$ bounds for UAV 1 for transmitting $\mathbf{\Lambda}_n$ using the event-based and fixed-rate communication schemes.

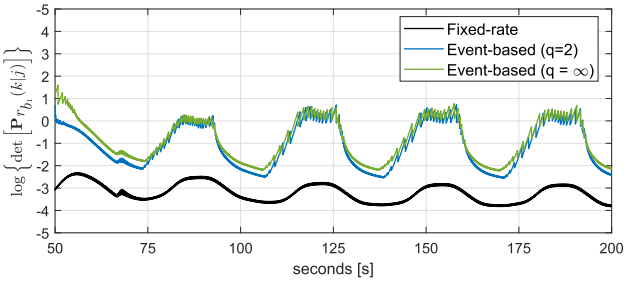

Fig. 8. Resulting logarithm of the determinant of the estimation error covariance for the position states of UAV 1 for the event-based and fixed-rate communication schemes, as well as the event-trigger threshold.

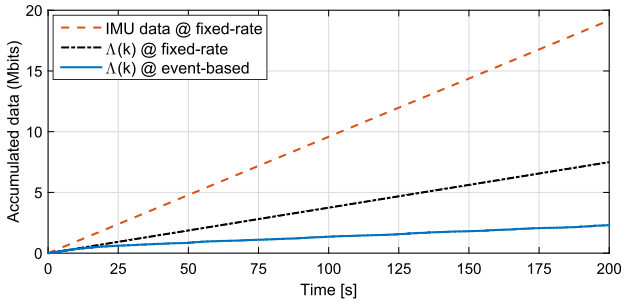

Fig. 9. Accumulation of the communicated data for transmitting IMU data, transmitting the packet $\mathbf{\Lambda}$ at a fixed-rate, and transmitting the packet $\mathbf{\Lambda}$ using the event-based communication scheme.

event-based communication schemes. The resulting accumulation of transmitted data for each scheme is illustrated in Fig. 9. Similar plots were noticed for the other three UAVs.

The following may be concluded from these plots. First, note from Fig. 7 that the estimation uncertainties associated with the event-based communication scheme are consistently larger than the ones produced by the fixed-rate scheme. This is due to skipped measurement updates when the test (22) is satisfied. Second, it can be seen that the UAV's position uncertainties reduce when the errors approach the trigger threshold, which causes all UAVs to transmit their data packets and perform an EKF update. The threshold is triggered only by the UAVs' vertical uncertainty, which is expected due to the large vertical dilution of precision due to all of the SOPs residing under the UAVs. Third, the degradation in estimation performance by skipping these measurements is captured by the distance between the corresponding $\pm 3\sigma$ bounds in Fig. 7 and by $\log\{\det[\mathbf{P}_{r_{b_1}}(k|j)]\}$ curves in Fig. 8. Fourth, it can be seen from Fig. 8 that event-triggering curves due to (22) and (31) result in larger uncertainty compared to fixed-rate triggering, as expected, with the ∞-norm being slightly larger than the 2-norm due to the less event triggering by the ∞-norm. Note that if a worst quality clock was equipped on the vehicles or SOPs, the error variances still appear bounded, however they would increase. A study on the CIRSLAM position error covariance for varying clock qualities was conducted in [52]. Finally, from Fig. 9, the following accumulation of transmitted data for each communication strategy was determined: 6.46 MB for transmitting $\mathbf{\Lambda}$ at a fixed-rate and 3.06 MB for transmitting $\mathbf{\Lambda}$ using the event-based scheme. Therefore, although using the event-based strategy to transmit $\mathbf{\Lambda}$ causes a small increase in position uncertainty, the accumulated transmitted data is reduced by 52.6% compared to transmitting $\mathbf{\Lambda}$ using fixed-rate scheme. Transmitting raw IMU data at a fixed-rate accumulated 18.6 MB of transmitted data. The event-based communication strategy reduces the required amount of transmitted data by 83.6% compared to transmitting raw IMU data.

VII. EXPERIMENTAL DEMONSTRATION

This section presents an experimental demonstration of the event-based communication scheme developed in Section VI using two UAVs equipped with consumer-grade IMUs and software-defined radios (SDRs).

A. Hardware and Software Setup

A consumer-grade L1 GPS active patch antenna [74] and an omnidirectional cellular antenna [75] were mounted on each UAV to acquire and track GPS signals and multiple cellular transmitters, respectively, whose signals were modulated through CDMA. The GPS and cellular signals were simultaneously downmixed and synchronously sampled via two-channel Ettus E312 universal software radio peripherals (USRPs). This data was then postprocessed through the Multichannel Adaptive TRansceiver Information eXtractor (MATRIX) SDR, which produced pseudorange measurements from all GPS L1 C/A signals in view and three cellular transmitters at 10 Hz [76]. The IMU data was sampled at 100 Hz from the UAVs' on-board proprietary navigation system, which was developed by Autel Robotics. The IMU data and pseudoranges were sent to a MATLAB-based CIRSLAM framework, which conducted the event testing,

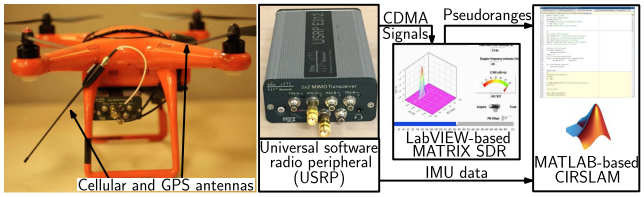

Fig. 10. Experiment hardware setup.

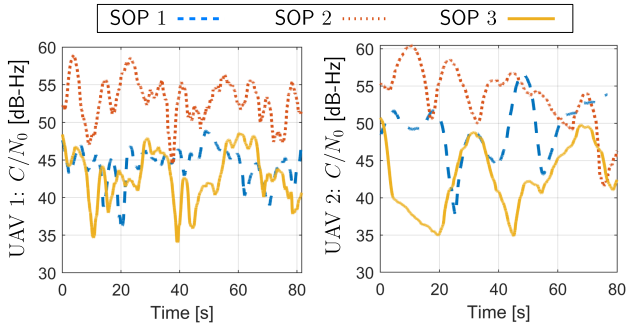

Fig. 11. Time history of received C/N_0 for UAV 1 and UAV 2 from SOP 1,2, and 3, produced by the MATRIX SDR.

emulated the packet transmissions $\{\Lambda_n\}_{n=1}^2$, and ran the EKF. Fig. 10 depicts the hardware and software setup.

In a real-time scenario, there will be a time difference between when pseudoranges are made by each vehicle and when all packets are received by other vehicles. This can cause an issue in traditional centralized EKFs, since the EKF time update requires the time difference between the previous EKF measurement update and the new measurement time for linearization. Since each vehicle may not be perfectly synchronized with other vehicles and the time when measurements arrive at the processor is not the time the measurements were made, linearization errors could accumulate. This would traditionally require maintaining the absolute time of all vehicles. However, in the proposed approach, the transmission of the packet $\mathbf{\Lambda}_n$ contains locally produced prior state estimates, which circumvents the need for each vehicle to maintain other vehicles' absolute time. Since the system is time-invariant, only the current measurement counter must be maintained and each vehicle must ensure that all packets are received from all other vehicles for the current measurement count. A small latency may be introduced to insure all measurements for a particular counter or batch of counters have arrived before performing the EKF measurement update. If a subset of measurements arrive after the EKF update is processed, then those measurements may be discarded to maintain estimation consensus with minimal degradation in performance, since the SOP CDMA pseudorange measurements are arriving at 10 Hz [58]. If the system designer decides to process the late measurements, a consensus algorithm should be ran. A vehicle in the system could be selected to maintain the measurement counter for the entire system. If that vehicle becomes unresponsive, a new vehicle could assume this responsibility.

B. CIRSLAM Initialization and Settings

The CIRSLAM framework was initialized using the following procedure. The state vector estimate was initialized according to

$$\hat{\boldsymbol{x}}(0|0)=\left[\hat{\boldsymbol{x}}_{\mathrm{r},1}^{\mathrm{T}}(0|0),\hat{\boldsymbol{x}}_{\mathrm{r},2}^{\mathrm{T}}(0|0),\hat{\boldsymbol{x}}_{\mathrm{sop},1}^{\mathrm{T}}(0|0),\ldots,\hat{\boldsymbol{x}}_{\mathrm{sop},3}^{\mathrm{T}}(0|0)\right]^{\mathrm{T}}$$

where the estimates of each UAV's orientation ${}_{g}^{b_n}\hat{\bar{\boldsymbol{q}}}(0|0)$, position $\hat{\boldsymbol{r}}_{b_n}(0|0)$, and velocity $\hat{\dot{\boldsymbol{r}}}_{b_n}(0|0)$ were set to values parsed from the beginning of the UAV's navigation system log files, which were recorded during the trajectory, and the IMU biases $\hat{\boldsymbol{b}}_{\mathrm{gyr},n}$ and $\hat{\boldsymbol{b}}_{\mathrm{acc},n}$ were initialized by averaging 5 s of gravity-compensated IMU measurements, while the vehicles were stationary and after their IMUs had warmed up. The cellular SOP transmitters' initial state estimates were drawn according to $\hat{\boldsymbol{x}}_{\mathrm{sop},m}(0|0)\sim\mathcal{N}([\boldsymbol{r}_{\mathrm{sop},m}^{\mathrm{T}},\boldsymbol{x}_{\mathrm{clk,sop},m}^{\mathrm{T}}(0)]^{\mathrm{T}},\mathbf{P}_{\mathrm{sop},m}(0|0))$. The true transmitters' positions $\{\boldsymbol{r}_{\mathrm{sop},m}\}_{m=1}^3$ were surveyed beforehand according to the framework described in [77] and verified using Google Earth. The initial clock bias and drift

$$\boldsymbol{x}_{\mathrm{clk,sop},m}(0)=c\left[\delta t_{\mathrm{sop},m}(0),\ \dot{\delta t}_{\mathrm{sop},m}(0)\right]^{\mathrm{T}}\quad m=1,\ldots,3$$

were solved for by using the initial set of cellular transmitter pseudoranges using (9) according to

$$c\delta t_{\mathrm{sop},m}(0)=\|\boldsymbol{r}_{b_n}(0)-\boldsymbol{r}_{\mathrm{sop},m}\|+c\delta t_{\mathrm{r},n}(0)-z_{\mathrm{sop},m}(0)$$
$$c\dot{\delta t}_{\mathrm{sop},m}(0)=[c\delta t_{\mathrm{sop},m}(1)-c\delta t_{\mathrm{sop},m}(0)]/T,$$

where $c\delta t_{\mathrm{sop},m}(1)=\|\boldsymbol{r}_{b_n}(1)-\boldsymbol{r}_{\mathrm{sop},m}\|+c\delta t_{\mathrm{r},n}(1)-{}^{n}z_{\mathrm{sop},m}(1)$ and the receiver's clock bias $c\delta t_{\mathrm{r},n}(0)$ and $c\delta t_{\mathrm{r},n}(1)$ was provided by the GPS receiver while GPS was available.

The corresponding estimation error covariance was initialized according to

$$\mathbf{P}_{\boldsymbol{x}}(0|0)=\mathrm{diag}\left[\mathbf{P}_{\boldsymbol{x}_{\mathrm{r}}}(0|0),\mathbf{P}_{\boldsymbol{x}_{\mathrm{sop},1}}(0|0),\ldots,\mathbf{P}_{\boldsymbol{x}_{\mathrm{sop},3}}(0|0)\right]$$
$$\mathbf{P}_{\boldsymbol{x}_{\mathrm{r}}}(0|0)=\mathrm{diag}\left[\mathbf{P}_{\boldsymbol{x}_{\mathrm{r},1}}(0|0),\mathbf{P}_{\boldsymbol{x}_{\mathrm{r},2}}(0|0)\right]$$
$$\mathbf{P}_{\boldsymbol{x}_{\mathrm{r},n}}(0|0)\triangleq\mathrm{diag}\left[\mathbf{P}_{\boldsymbol{x}_{\mathrm{imu},n}}(0|0),\ \mathbf{P}_{\boldsymbol{x}_{\mathrm{clk,r},n}}(0|0)\right]$$
$$\mathbf{P}_{\boldsymbol{x}_{\mathrm{imu},n}}(0|0)\equiv\mathrm{diag}\left[(0.1)\cdot\mathbf{I}_{3\times3},\ 9\cdot\mathbf{I}_{3\times3},\ \mathbf{I}_{3\times3},\ \left(10^{-4}\right)\cdot\mathbf{I}_{6\times6}\right]$$
$$\mathbf{P}_{\boldsymbol{x}_{\mathrm{clk,r},n}}(0|0)\equiv\mathrm{diag}\left[0.1,\ 0.01\right]\quad n=1,2$$
$$\mathbf{P}_{\mathrm{sop},m}(0|0)\equiv10^3\cdot\mathrm{diag}\left[\mathbf{I}_{3\times3},0.3,0.03\right],\quad m=1,2,3.$$

The process noise covariance of the receiver's clock $\mathbf{Q}_{\mathrm{clk,r},n}$ was set to correspond to a typical TCXO. The process noise covariances of the cellular transmitters' clocks were set to correspond to a typical OCXO, which is usually the case for cellular transmitters [78]. The power spectral density matrices associated with the gyroscope and accelerometer noise were set to $\mathbf{S}_{\boldsymbol{n}_{\mathrm{gyr}}}\equiv\left(7\times10^{-4}\right)^2\cdot\mathbf{I}_{3\times3}$ and $\mathbf{S}_{\boldsymbol{n}_{\mathrm{acc}}}\equiv\left(5\times10^{-4}\right)^2\cdot\mathbf{I}_{3\times3}$, respectively. The power spectral density matrices associated with the gyroscope and accelerometer bias variations were set to $\mathbf{S}_{\boldsymbol{w}_{\mathrm{gyr}}}\equiv\left(1\times10^{-4}\right)^2\cdot\mathbf{I}_{3\times3}\,\mathbf{S}_{\boldsymbol{w}_{\mathrm{acc}}}\equiv\left(1\times10^{-4}\right)^2\cdot\mathbf{I}_{3\times3}$, whose values were found empirically using raw IMU data. The measurement noise variances $\{{}^{n}\sigma_{\mathrm{sop},m}^2\}_{m=1}^3$ for UAV $n\in\{1,2\}$ were time-varying, and calculated according to (42), except that $t_{\mathrm{eml}}\equiv1$, ${}^{n}\sigma_{\mathrm{sv},l,j}^2$ is replaced with ${}^{n}\sigma_{\mathrm{sop},m,j}^2$, $T_c\equiv$

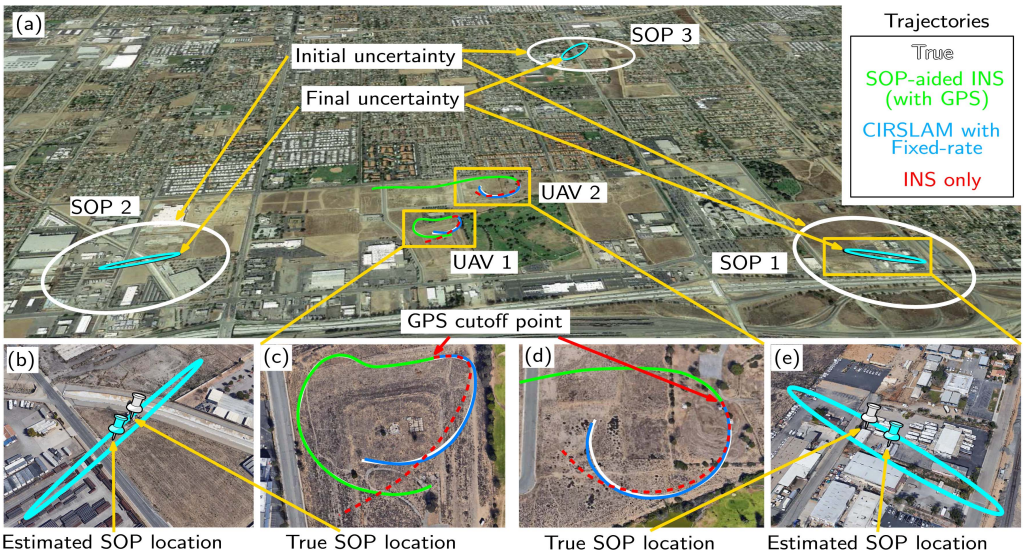

Fig. 12. (a) Experimental environment with three cellular SOPs and two UAVs. (b)–(e) Mapping and navigation results for CIRSLAM with fixed transmission rate.

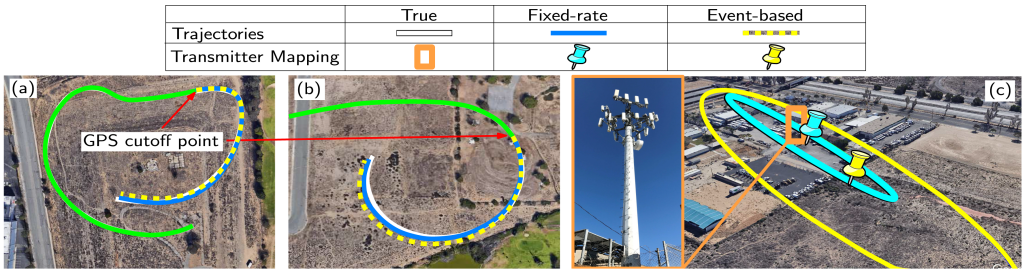

Fig. 13. (a)–(b) UAV navigation results for fixed-rate (blue solid) and event-based (yellow dashed) information fusion. (c) Mapping results for SOP 1 using fixed-rate (blue) and event-based (yellow) information fusion.

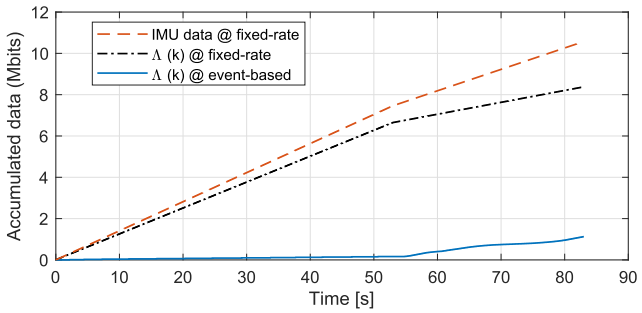

Fig. 14. Accumulation of the communicated data for transmitting IMU data, transmitting the packet $\mathbf{\Lambda}$ at a fixed-rate, and transmitting the packet $\mathbf{\Lambda}$ using the event-based communication scheme during the experiment.

$1/(1.2288 \times 10^6)$, $\sigma_s \equiv 10$, $T_{CO} \equiv 1/37.5$ s, and the carrier-to-noise ratios $\{{}^n(C/N_0)_{m,j}\}_{m=1}^3$, $n \in \{1, 2\}$, are replaced with the received carrier-to-noise ratio estimated by the MATRIX SDR, which are plotted in Fig. 11.

C. Experimental Results

The UAVs traversed the white trajectories in Fig. 12(c) and (d), in which GPS was available for the first 50 s then unavailable for the last 30 s. To collaboratively estimate these trajectories, the CIRSLAM framework was used and two transmission strategies were studied: 1) event-based using (22) with $\xi_{\max} \equiv 20$ m and $p \equiv 0.95$, and for a comparative analysis, 2) fixed-rate where τ is closed periodically with a period of 0.2 s (see Fig. 1). The estimated trajectories using each transmission scheme for UAV 1 and UAV 2 are plotted in Fig. 13(a) and (b), respectively. The north-east RMSEs and final errors for each communication scheme for the UAVs are summarized in Table I. The final estimated transmitter location and corresponding 99$^{\text{th}}$-percentile north-east uncertainty ellipse of SOP 1 for each communication strategy are plotted in Fig. 13(c). Notice from I, the fixed-rate RMSE and the final error are significantly lower compared to an INS-only after the GPS cutoff point (unaided-INS). If a visual inertial odometry (VIO) system is used instead of an INS, one can expect similar RMSEs of 3–5 m [79]. From the plots in Fig. 13,

TABLE I
Estimation Errors: Unaided-INS Versus SOP-Aided INS With Fixed-Rate and Event-Based Communication

Scheme	Unaided-INS		Fixed-rate		Event-based	
Vehicle	UAV 1	UAV 2	UAV 1	UAV 2	UAV 1	UAV 2
Pos. RMSE (m)	21.5	18.9	3.1	4.2	4.3	6.3
Final Error (m)	57.3	54.7	4.3	6.0	6.1	8.0

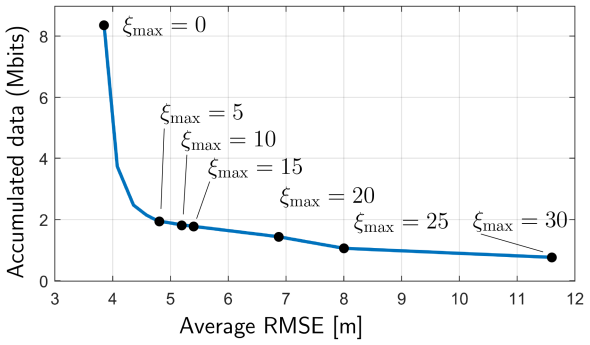

Fig. 15. Accumulated transmitted data versus the average RMSE between UAV 1 and UAV 2 when using the event-based communication scheme with $p = 0.95$ and a varying $\xi_{\max}$.

one can note a slight degradation in UAV localization performance when comparing the event-based with fixed-rate schemes; however, the event-based scheme maintained the specified constraints p and $\boldsymbol{\xi}_{\max}$ and the amount of transmitted data was reduced.

To visualize the amount of transmitted data, the accumulated data for each strategy transmitted by each UAV is plotted as a function of time in Fig. 14. For a comparative analysis, the accumulated data for transmitting raw IMU data at a fixed rate is also plotted. In order to calculate the accumulated data associated with transmitting $\boldsymbol{\Lambda}$, the size of $\boldsymbol{\Lambda}$ in bits was found by summing the number of values in (14) and setting each value to be a 32-bit float data type, as described in [58]. It can be seen from Fig. 14 that transmitting $\boldsymbol{\Lambda}$ at a fixed rate required the transmission of 8.38 Mbits, whereas transmitting $\boldsymbol{\Lambda}$ using an event-based strategy reduced the transmission to 1.12 Mbits, a 86.6% reduction. If raw IMU data was transmitted at a fixed rate instead of the packet $\boldsymbol{\Lambda}$, the accumulated data was found to be 10.6 Mbits.

To study the tradeoff between the accumulated data savings and the position estimate RMSE, the same data was passed through the CIRSLAM framework for several runs, where each run used a different user-specified max error $\xi_{\max}$. Specifically, the probability was set to $p \equiv 0.95$ and the max error was swept from $\xi_{\max} \equiv 0$ to $\xi_{\max} \equiv 30$. For each run, the RMSEs for UAV 1 and UAV 2 were averaged. The resulting accumulated transmitted data versus average RMSE curve is plotted in Fig. 15. Notice from Fig. 15 that when $\xi_{\max} \equiv 0$, the average RMSE and the accumulated transmitted data are equal to the values found for the fixed-rate scheme. This is due to $\xi_{\max} \equiv 0$ causing the event-based scheme to transmit at the fixed rate of measurements arriving. From $\xi_{\max} \equiv 0$ to $\xi_{\max} \equiv 5$, the data savings are approximately exponential with increasing RMSE. After $\xi_{\max} \equiv 5$, the data savings are approximately linear with increasing RMSE, with a rate of 0.172 Mbits per meter.

VIII. CONCLUSION

This article developed and studied event-based communication strategies for navigating vehicles collaboratively aiding their INSs' with shared measurements. These strategies aimed to reduce the accumulated shared data between collaborators, while maintaining a specified vehicle positioning error with probability p. The inequalities (22) and (31) provide simple tests to determine if the specified constraints will be violated and trigger communication of $\boldsymbol{\Lambda}_n$. The pdf of $\|\tilde{\boldsymbol{r}}_{b_n}\|^2_{\mathrm{M}}$ was characterized, which enabled computing the threshold that satisfies a specified p. Simulation and experimental results demonstrating the event-based communication strategy with specified constraints were presented. The experimental results demonstrated that the event-based communication strategy could reduce the amount of accumulated data by 86.6% compared to communicating at a fixed-rate, while maintaining the user-specified UAV position estimation error constraint.

APPENDIX A
INS STATE TRANSITION AND PROCESS NOISE COVARIANCE MATRICES

The calculation of the discrete-time linearized INS state transition matrix $\boldsymbol{\Phi}_{\mathrm{ins},n}$ and process noise covariance $\mathbf{Q}_{\mathrm{ins},n}$ are performed using strapdown INS equations (2)–(3) resolved in an ECI frame as described in [56], [57]. The matrix $\boldsymbol{\Phi}_{\mathrm{ins},n}$ is given by

$$\boldsymbol{\Phi}_{\mathrm{ins},n}(i) = \begin{bmatrix} \mathbf{I}_{3\times3} & \mathbf{0}_{3\times3} & \mathbf{0}_{3\times3} & \boldsymbol{\Phi}_{\bar{\boldsymbol{q}}\boldsymbol{b}_{\mathrm{gyr}},n} & \mathbf{0}_{3\times3} \\ \boldsymbol{\Phi}_{\boldsymbol{r}\bar{\boldsymbol{q}},n} & \mathbf{I}_{3\times3} & T\mathbf{I}_{3\times3} & \boldsymbol{\Phi}_{\boldsymbol{r}\boldsymbol{b}_{\mathrm{gyr}},n} & \boldsymbol{\Phi}_{\boldsymbol{r}\boldsymbol{b}_{\mathrm{acc}},n} \\ \boldsymbol{\Phi}_{\dot{\boldsymbol{r}}\bar{\boldsymbol{q}},n} & \mathbf{0}_{3\times3} & \mathbf{I}_{3\times3} & \boldsymbol{\Phi}_{\dot{\boldsymbol{r}}\boldsymbol{b}_{\mathrm{gyr}},n} & \boldsymbol{\Phi}_{\dot{\boldsymbol{r}}\boldsymbol{b}_{\mathrm{acc}},n} \\ \mathbf{0}_{3\times3} & \mathbf{0}_{3\times3} & \mathbf{0}_{3\times3} & \mathbf{I}_{3\times3} & \mathbf{0}_{3\times3} \\ \mathbf{0}_{3\times3} & \mathbf{0}_{3\times3} & \mathbf{0}_{3\times3} & \mathbf{0}_{3\times3} & \mathbf{I}_{3\times3} \end{bmatrix}$$

$$\boldsymbol{\Phi}_{\bar{\boldsymbol{q}}\boldsymbol{b}_{\mathrm{gyr}},n} = -\frac{T}{2}\left[\hat{\mathbf{R}}_n^{\mathsf{T}}(i+1) + \hat{\mathbf{R}}_n^{\mathsf{T}}(i)\right]$$

$$\boldsymbol{\Phi}_{\dot{\boldsymbol{r}}\bar{\boldsymbol{q}},n} = -\frac{T}{2}\lfloor[\hat{\boldsymbol{a}}_n(i) + \hat{\boldsymbol{a}}_n(i+1)]\times\rfloor, \quad \boldsymbol{\Phi}_{\boldsymbol{r}\bar{\boldsymbol{q}},n} = \frac{T}{2}\boldsymbol{\Phi}_{\dot{\boldsymbol{r}}\bar{\boldsymbol{q}},n}$$

$$\boldsymbol{\Phi}_{\dot{\boldsymbol{r}}\boldsymbol{b}_{\mathrm{gyr}},n} = -\frac{T}{2}\lfloor\hat{\boldsymbol{a}}_n(i)\times\rfloor\boldsymbol{\Phi}_{\bar{\boldsymbol{q}}\boldsymbol{b}_{\mathrm{gyr}},n}, \quad \boldsymbol{\Phi}_{\dot{\boldsymbol{r}}\boldsymbol{b}_{\mathrm{acc}},n} = \boldsymbol{\Phi}_{\bar{\boldsymbol{q}}\boldsymbol{b}_{\mathrm{gyr}},n}$$

$$\boldsymbol{\Phi}_{\boldsymbol{r}\boldsymbol{b}_{\mathrm{gyr}},n} = \frac{T}{2}\boldsymbol{\Phi}_{\dot{\boldsymbol{r}}\boldsymbol{b}_{\mathrm{gyr}},n}, \quad \boldsymbol{\Phi}_{\boldsymbol{r}\boldsymbol{b}_{\mathrm{acc}},n} = \frac{T}{2}\boldsymbol{\Phi}_{\dot{\boldsymbol{r}}\boldsymbol{b}_{\mathrm{acc}},n}$$

where $\hat{\mathbf{R}}_n(i) \triangleq \mathbf{R}\left[{}^{b_n}_{g}\hat{\bar{\boldsymbol{q}}}(i|j)\right]$ is the equivalent rotation matrix of ${}^{b_n}_{g}\hat{\bar{\boldsymbol{q}}}(i|j)$, which is the estimate of ${}^{b_n}_{g}\bar{\boldsymbol{q}}(i)$ using all measurements up to time-step j; $\hat{\boldsymbol{a}}_n(i) \triangleq \hat{\mathbf{R}}_n^{\mathsf{T}}(i)[{}^{n}\boldsymbol{a}_{\mathrm{imu}}(i) - \hat{\boldsymbol{b}}_{\mathrm{acc},n}(i|j)]$, where $\hat{\boldsymbol{b}}_{\mathrm{acc},n}(i|j)$ is the estimate of $\boldsymbol{b}_{\mathrm{acc},n}(i)$ using all measurements up to time-step j; and $\lfloor(\cdot)\times\rfloor$ is the skew-symmetric matrix obtained according to (15). The discrete-time linearized INS process noise covariance $\mathbf{Q}_{\mathrm{ins},n}$ is given by

$$\mathbf{Q}_{\mathrm{ins},n}(i) = \frac{T}{2}\boldsymbol{\Phi}_{\mathrm{ins},n}(i)\mathbf{N}_{c,n}\boldsymbol{\Phi}_{\mathrm{ins},n}^{\mathsf{T}}(i) + \mathbf{N}_{c,n}$$

$$\mathbf{N}_{c,n} = \mathrm{diag}\left[\mathbf{S}_{\boldsymbol{n}_{\mathrm{gyr}},n},\ \mathbf{0}_{3\times3},\ \mathbf{S}_{\boldsymbol{n}_{\mathrm{acc}},n},\ \mathbf{S}_{\boldsymbol{w}_{\mathrm{gyr}},n},\ \mathbf{S}_{\boldsymbol{w}_{\mathrm{acc}},n}\right]$$

where $\mathbf{S}_{\boldsymbol{n}_{\mathrm{gyr}},n} = T\mathbf{Q}_{\boldsymbol{n}_{\mathrm{gyr}},n}$ and $\mathbf{S}_{\boldsymbol{n}_{\mathrm{acc}},n} = T\mathbf{Q}_{\boldsymbol{n}_{\mathrm{acc}},n}$ are the PSD matrices of the gyroscope's and accelerometer's random noise, respectively, and $\mathbf{S}_{\boldsymbol{w}_{\mathrm{gyr}},n} = \mathbf{Q}_{\boldsymbol{w}_{\mathrm{gyr}},n}/T$ and $\mathbf{S}_{\boldsymbol{w}_{\mathrm{acc}},n} = \mathbf{Q}_{\boldsymbol{w}_{\mathrm{acc}},n}/T$ are the PSD matrices of the gyroscope's and accelerometer's bias variation, respectively, which may

be derived from values obtained from IMU specification sheets.

APPENDIX B

INS STATE TRANSITION MATRIX APPROXIMATION

After a κ-step propagation, the INS state transition matrix takes a simple form, which can be approximated as [58]

$$\boldsymbol{\Phi}_{\text{ins},n}(k,\, j) \approx \begin{bmatrix} \mathbf{I}_{3\times3} & \mathbf{0}_{3\times3} & \mathbf{0}_{3\times3} & \kappa T\mathbf{R}[\bar{\boldsymbol{q}}_{1,n}] & \mathbf{0}_{3\times3} \\ \lfloor \boldsymbol{v}_{1,n}\times \rfloor & \mathbf{I}_{3\times3} & \mathbf{I}_{3\times3}T & \boldsymbol{\Phi}_{1,n} & \frac{\kappa T^2}{2}\mathbf{R}[\bar{\boldsymbol{q}}_{2,n}] \\ \lfloor \boldsymbol{v}_{2,n}\times \rfloor & \mathbf{0}_{3\times3} & \mathbf{I}_{3\times3} & \boldsymbol{\Phi}_{2,n} & \kappa T\mathbf{R}[\bar{\boldsymbol{q}}_{1,n}] \\ \mathbf{0}_{3\times3} & \mathbf{0}_{3\times3} & \mathbf{0}_{3\times3} & \mathbf{I}_{3\times3} & \mathbf{0}_{3\times3} \\ \mathbf{0}_{3\times3} & \mathbf{0}_{3\times3} & \mathbf{0}_{3\times3} & \mathbf{0}_{3\times3} & \mathbf{I}_{3\times3} \end{bmatrix} \tag{43}$$

where $\kappa = k - j$; $\lfloor \boldsymbol{v}_{1,n}\times \rfloor \in \mathbb{R}^{3\times3}$ and $\lfloor \boldsymbol{v}_{2,n}\times \rfloor \in \mathbb{R}^{3\times3}$ are skew symmetric matrices whose elements are defined from the vectors $\boldsymbol{v}_{1,n} \in \mathbb{R}^3$ and $\boldsymbol{v}_{2,n} \in \mathbb{R}^3$, respectively; the matrices $\mathbf{R}[\bar{\boldsymbol{q}}_{1,n}] \in \mathbb{R}^{3\times3}$ and $\mathbf{R}[\bar{\boldsymbol{q}}_{2,n}] \in \mathbb{R}^{3\times3}$ are rotation matrices; and $\boldsymbol{\Phi}_{1,n} \in \mathbb{R}^{3\times3}$ and $\boldsymbol{\Phi}_{1,n} \in \mathbb{R}^{3\times3}$ are arbitrarily structured matrices.

Note the following two properties of the structure (43). First, since $\lfloor \boldsymbol{v}_{1,n}\times \rfloor$ and $\lfloor \boldsymbol{v}_{2,n}\times \rfloor$ maintain a skew symmetric form, they can be transmitted using only three elements each. Second, the scaling pre-multiplying the matrices $\mathbf{R}[\bar{\boldsymbol{q}}_{1,n}]$ and $\mathbf{R}[\bar{\boldsymbol{q}}_{2,n}]$ is deterministic and only dependent on the IMU sampling period T and the number of iterations κ; therefore, these matrices can be converted to quaternions $\bar{\boldsymbol{q}}_{1,n}$ and $\bar{\boldsymbol{q}}_{2,n}$ and then transmitted using only four elements each. From these properties, the sufficient INS information to package for transmission is found to be

$$\boldsymbol{\Lambda}_{\text{ins},n} \triangleq \left\{ \boldsymbol{v}_{1,n},\, \boldsymbol{v}_{2,n},\, \bar{\boldsymbol{q}}_{1,n},\, \bar{\boldsymbol{q}}_{2,n},\, \boldsymbol{\Phi}_{1,n},\, \boldsymbol{\Phi}_{2,n} \right\}$$

which only requires the transmission of 32 floating-point values every EKF measurement update.

APPENDIX C

EKF STATE MEASUREMENT UPDATE EQUATIONS

When the orientation of the vehicle is modeled using quaternions, the standard EKF equations are modified to deal with the 3-D orientation error correction, which contains one less dimension than the 4-D orientation quaternion estimate. Specifically, the quaternion estimate corresponding to each vehicle's orientation is updated using quaternion multiplication and all other estimates are updated using standard additive EKF update equations. To this end, define the state estimate vector as

$$\hat{\boldsymbol{x}} \triangleq \left[\hat{\boldsymbol{x}}_{\text{r},1}^{\mathsf{T}}, \ldots, \hat{\boldsymbol{x}}_{\text{r},N}^{\mathsf{T}},\, \hat{\boldsymbol{x}}_{\text{sop},1}^{\mathsf{T}}, \ldots, \hat{\boldsymbol{x}}_{\text{sop},M}^{\mathsf{T}} \right]^{\mathsf{T}}.$$

The state estimate of each vehicle is separated into two parts according to $\hat{\boldsymbol{x}}_{\text{r},n} \triangleq [{}_g^{b_n}\hat{\boldsymbol{q}}^{\mathsf{T}}, \hat{\boldsymbol{y}}_n^{\mathsf{T}}]^{\mathsf{T}}$, where ${}_g^{b_n}\hat{\boldsymbol{q}} \in \mathbb{R}^4$ is the orientation quaternion estimate and $\hat{\boldsymbol{y}} \in \mathbb{R}^{14}$ is a vector containing the remaining estimates of $\boldsymbol{x}_{\text{r},n}$.

Next, define the EKF correction vector as

$$\check{\boldsymbol{x}} \triangleq \left[\check{\boldsymbol{x}}_{\text{r},1}^{\mathsf{T}}, \ldots, \check{\boldsymbol{x}}_{\text{r},N}^{\mathsf{T}},\, \check{\boldsymbol{x}}_{\text{sop},1}^{\mathsf{T}}, \ldots, \check{\boldsymbol{x}}_{\text{sop},M}^{\mathsf{T}} \right]^{\mathsf{T}}$$

where $\check{\boldsymbol{x}}_{\text{r},n} \triangleq [\check{\boldsymbol{\theta}}_n^{\mathsf{T}}, \check{\boldsymbol{y}}_n^{\mathsf{T}}]^{\mathsf{T}}$ and $\check{\boldsymbol{\theta}}_n \in \mathbb{R}^3$ is the orientation correction and $\check{\boldsymbol{y}}_n \in \mathbb{R}^{14}$ is a vector containing the remaining corrections for the vehicle nth.

The EKF correction vector $\check{\boldsymbol{x}}(k)$, which is to be applied to the current state prediction $\hat{\boldsymbol{x}}(k|j)$ to produce the EKF state measurement update $\hat{\boldsymbol{x}}(k|k)$, is computed according to

$$\check{\boldsymbol{x}}(k) = \mathbf{K}(k)\boldsymbol{\nu}(k|j)$$

where $\boldsymbol{\nu}(k|j) \triangleq \boldsymbol{z}(k) - \hat{\boldsymbol{z}}(k|j)$ is the measurement residual, $\mathbf{K} = \mathbf{L}\mathbf{S}^{-1}$, and $\mathbf{L}$ and $\mathbf{S}$ are defined in (17) and (18), respectively. Finally, the EKF state measurement update $\hat{\boldsymbol{x}}(k|k)$ is computed by applying $\check{\boldsymbol{\theta}}_n(k)$ to ${}_g^{b_n}\hat{\boldsymbol{q}}(k|j)$ and $\check{\boldsymbol{y}}(k)$ to $\boldsymbol{y}_n(k|j)$ for each vehicle $n = 1, \ldots, N$, using

$$\hat{\boldsymbol{x}}(k|k) = \begin{bmatrix} {}_g^{b_n}\hat{\boldsymbol{q}}(k|j) \otimes \left[\frac{1}{2}\check{\boldsymbol{\theta}}_n^{\mathsf{T}}(k),\, \sqrt{1 - \frac{1}{4}\check{\boldsymbol{\theta}}_n^{\mathsf{T}}(k)\check{\boldsymbol{\theta}}_n(k)} \right]^{\mathsf{T}} \\ \hat{\boldsymbol{y}}_n(k|j) + \check{\boldsymbol{y}}_n(k) \end{bmatrix}$$

and applying $\check{\boldsymbol{x}}_{\text{sop},n}$ to each SOP $m = 1, \ldots, M$, using

$$\hat{\boldsymbol{x}}_{\text{sop},n}(k|k) = \hat{\boldsymbol{x}}_{\text{sop},n}(k|j) + \check{\boldsymbol{x}}_{\text{sop},n}(k).$$

ACKNOWLEDGMENT

The authors would like to thank Yanhao Yang for insightful discussions.

REFERENCES

[1] S. Zhao, Y. Chen, and J. Farrell, "High-precision vehicle navigation in urban environments using an MEM's IMU and single-frequency GPS receiver," *IEEE Trans. Intell. Transp. Syst.*, vol. 17, no. 10, pp. 2854–2867, Oct. 2016.

[2] M. Atia et al., "A low-cost lane-determination system using GNSS/IMU fusion and HMM-based multistage map matching," *IEEE Trans. Intell. Transp. Syst.*, vol. 18, no. 11, pp. 3027–3037, Nov. 2017.

[3] D. Venable and J. Raquet, "Large scale image aided navigation," *IEEE Trans. Aerosp. Electron. Syst.*, vol. 52, no. 6, pp. 2849–2860, Dec. 2016.

[4] C. Hu, Y. Chen, and J. Wang, "Fuzzy observer-based transitional path-tracking control for autonomous vehicles," *IEEE Trans. Intell. Transp. Syst.*, vol. 22, no. 5, pp. 3078–3088, May 2021.

[5] A. Soloviev, "Tight coupling of GPS, INS, and laser for urban navigation," *IEEE Trans. Aerosp. Electron. Syst.*, vol. 46, no. 4, pp. 1731–1746, Oct. 2010.

[6] R. Opromolla, G. Fasano, G. Rufino, and M. Grassi, "Pose estimation for spacecraft relative navigation using model-based algorithms," *IEEE Trans. Aerosp. Electron. Syst.*, vol. 53, no. 1, pp. 431–447, Feb. 2017.

[7] C. Cadena et al., "Past, present, and future of simultaneous localization and mapping: Toward the robust-perception age," *IEEE Trans. Robot.*, vol. 32, no. 6, pp. 1309–1332, Dec. 2016.

[8] T. Qin, P. Li, and S. Shen, "VINS-mono: A robust and versatile monocular visual-inertial state estimator," *IEEE Trans. Robot.*, vol. 34, no. 4, pp. 1004–1020, Aug. 2018.

[9] G. Einicke, "High-order filtering of LIDAR data to assist coal shiploading," *IEEE Trans. Aerosp. Electron. Syst.*, vol. 53, no. 3, pp. 1481–1488, Jun. 2017.

[10] J. Raquet et al., "Position, navigation, and timing technologies in the 21st century," *Part D: Position, Navigation, and Timing Using Radio Signals-of-Opportunity*, J. Morton, F. van Diggelen, J. Spilker Jr., and B. Parkinson, Eds. vol. 2. Hoboken, NJ, USA: Wiley, 2021, ch. 35–43, pp. 1115–1412.

[11] X. Chen, Q. Wei, F. Wang, Z. Jun, S. Wu, and A. Men, "Super-resolution time of arrival estimation for a symbiotic FM radio data system," *IEEE Trans. Broadcast.*, vol. 66, no. 4, pp. 847–856, Dec. 2020.

[12] J. Khalife and Z. Kassas, "Navigation with cellular CDMA signals–Part II: Performance analysis and experimental results," *IEEE Trans. Signal Process.*, vol. 66, no. 8, pp. 2204–2218, Apr. 2018.

[13] J. del Peral-Rosado, J. López-Salcedo, F. Zanier, and G. Seco-Granados, "Position accuracy of joint time-delay and channel estimators in LTE networks," *IEEE Access*, vol. 6, pp. 25185–25199, 2018.

[14] T. Kang, H. Lee, and J. Seo, "TOA-based ranging method using CRS in LTE signals," *J. Adv. Navigation Technol.*, vol. 23, no. 5, pp. 437–443, Oct. 2019.

[15] P. Wang and Y. Morton, "Multipath estimating delay lock loop for LTE signal TOA estimation in indoor and urban environments," *IEEE Trans. Wireless Commun.*, vol. 19, no. 8, pp. 5518–5530, Aug. 2020.

[16] J. Gante, L. Sousa, and G. Falcao, "Dethroning GPS: Low-power accurate 5G positioning systems using machine learning," *IEEE Trans. Emerg. Sel. Topics Circuits Syst.*, vol. 10, no. 2, pp. 240–252, Jun. 2020.

[17] H. Dun, C. Tiberius, and G. Janssen, "Positioning in a multipath channel using OFDM signals with carrier phase tracking," *IEEE Access*, vol. 8, pp. 13011–13028, 2020.

[18] A. Abdallah and Z. Kassas, "UAV navigation with 5G carrier phase measurements," in *Proc. 34th Int. Tech. Meeting Satell. Division Inst. Navigation Conf.*, 2021, pp. 3294–3306.

[19] J. Yang, X. Wang, M. Rahman, S. Park, H. Kim, and Y. Wu, "A new positioning system using DVB-T2 transmitter signature waveforms in single frequency networks," *IEEE Trans. Broadcast.*, vol. 58, no. 3, pp. 347–359, Sep. 2012.

[20] L. Chen, P. Thevenon, G. Seco-Granados, O. Julien, and H. Kusniemi, "Analysis on the TOA tracking with DVB-T signals for positioning," *IEEE Trans. Broadcast.*, vol. 62, no. 4, pp. 957–961, Dec. 2016.

[21] C. Yang and A. Soloviev, "Mobile positioning with signals of opportunity in urban and urban canyon environments," in *Proc. IEEE/ION Position, Location, Navigation Symp.*, 2020, pp. 1043–1059.

[22] T. Reid, A. Neish, T. Walter, and P. Enge, "Broadband LEO constellations for navigation," *NAVIGATION J. Inst. Navigation*, vol. 65, no. 2, pp. 205–220, 2018.

[23] H. Benzerrouk, Q. Nguyen, F. Xiaoxing, A. Amrhar, A. Nebylov, and R. Landry, "Alternative PNT based on iridium next LEO satellites Doppler/INS integrated navigation system," in *Proc. Saint Petersburg Int. Conf. Integr. Navigation Syst.*, 2019, pp. 1–10.

[24] S. Kozhaya, J. Haidar-Ahmad, A. Abdallah, Z. Kassas, and S. Saab, "Comparison of neural network architectures for simultaneous tracking and navigation with LEO satellites," in *Proc. 34th Int. Tech. Meeting Satell. Division Inst. Navigation Conf.*, 2021, pp. 2507–2520.

[25] Z. Kassas et al., "Enter LEO on the GNSS stage: Navigation with starlink satellites," *Inside GNSS Mag.*, vol. 16, no. 6, pp. 42–51, 2021.

[26] Z. Kassas, J. Morales, K. Shamaei, and J. Khalife, "LTE steers UAV," *GPS World Mag.*, vol. 28, no. 4, pp. 18–25, Apr. 2017.

[27] J. Morales and Z. Kassas, "Tightly-coupled inertial navigation system with signals of opportunity aiding," *IEEE Trans. Aerosp. Electron. Syst.*, vol. 57, no. 3, pp. 1930–1948, Jun. 2021.

[28] J. Morales, J. Khalife, and Z. Kassas, "GNSS vertical dilution of precision reduction using terrestrial signals of opportunity," in *Proc. ION Int. Tech. Meeting Conf.*, 2016, pp. 664–669.

[29] Z. Kassas and T. Humphreys, "Observability analysis of collaborative opportunistic navigation with pseudorange measurements," *IEEE Trans. Intell. Transp. Syst.*, vol. 15, no. 1, pp. 260–273, Feb. 2014.

[30] C. Yang and A. Soloviev, "Simultaneous localization and mapping of emitting radio sources-SLAMERS," in *Proc. 28th Int. Tech. Meeting Satell. Division Inst. Navigation Conf.*, 2015, pp. 2343–2354.

[31] C. Yang and A. Soloviev, "Positioning with mixed signals of opportunity subject to multipath and clock errors in urban mobile fading environments," in *Proc. 31th Int. Tech. Meeting Satell. Division Inst. Navigation Conf.*, 2018, pp. 223–243.

[32] N. Alam, A. Kealy, and A. Dempster, "Cooperative inertial navigation for GNSS-challenged vehicular environments," *IEEE Trans. Intell. Transp. Syst.*, vol. 14, no. 3, pp. 1370–1379, Sep. 2013.

[33] C. Yang and A. Soloviev, "Covariance analysis of spatial and temporal effects of collaborative navigation," *NAVIGATION J. Inst. Navigation*, vol. 61, no. 3, pp. 213–225, 2014.

[34] H. Mokhtarzadeh and D. Gebre-Egziabher, "Cooperative inertial navigation," *NAVIGATION J. Inst. Navigation*, vol. 61, no. 2, pp. 77–94, 2014.

[35] N. Souli, R. Makrigiorgis, P. Kolios, and G. Ellinas, "Real-time relative positioning system implementation employing signals of opportunity, inertial, and optical flow modalities," in *Proc. Int. Conf. Unmanned Aircr. Syst.*, 2021, pp. 229–236.

[36] N. Souli, P. Kolios, and G. Ellinas, "Online relative positioning of autonomous vehicles using signals of opportunity," *IEEE Trans. Intell. Veh.*, vol. 7, no. 4, pp. 873–885, Dec. 2022.

[37] Y. Wang and X. Li, "Distributed estimation fusion with unavailable cross-correlation," *IEEE Trans. Aerosp. Electron. Syst.*, vol. 48, no. 1, pp. 259–278, Jan. 2012.

[38] L. Carrillo-Arce, E. Nerurkar, J. Gordillo, and S. Roumeliotis, "Decentralized multi-robot cooperative localization using covariance intersection," in *Proc. IEEE/RSJ Int. Conf. Intell. Robots Syst.*, 2013, pp. 1412–1417.

[39] H. Li, F. Nashashibi, and M. Yang, "Split covariance intersection filter: Theory and its application to vehicle localization," *IEEE Trans. Intell. Transp. Syst.*, vol. 14, no. 4, pp. 1860–1871, Dec. 2013.

[40] H. Mokhtarzadeh and D. Gebre-Egziabher, "Performance of networked dead reckoning navigation system," *IEEE Trans. Aerosp. Electron. Syst.*, vol. 52, no. 5, pp. 2539–2553, Oct. 2016.

[41] J. Zhu and S. Kia, "Cooperative localization under limited connectivity," *IEEE Trans. Robot.*, vol. 35, no. 6, pp. 1523–1530, Dec. 2019.

[42] A. Coluccia and A. Fascista, "A review of advanced localization techniques for crowdsensing wireless sensor networks," *Sensors*, vol. 19, no. 5, pp. 988–1017, 2019.

[43] S. Trimpe and R. D'Andrea, "Event-based state estimation with variance-based triggering," *IEEE Trans. Autom. Control*, vol. 59, no. 12, pp. 3266–3281, Dec. 2014.

[44] S. Kia, J. Cortes, and S. Martinez, "Distributed event-triggered communication for dynamic average consensus in networked systems," *Automatica*, vol. 59, pp. 112–119, Sep. 2015.

[45] Q. Liu, Z. Wang, and X. He, *Stochastic Control and Filtering Over Constrained Communication Networks. Studies in Systems, Decision and Control. Event-Based Recursive Distributed Filtering*. Berlin, Germany: Springer, 2019, ch. 7, pp. 117–134.

[46] Y. Yilmax, G. Moustakides, and X. Wang, "Spectrum sensing via event-triggered sampling," in *Proc. Asilomar Conf. Signals, Syst., Comput.*, 2011, pp. 1420–1424.

[47] C. Yang, L. Shi, and W. Ma, "A study of estimation and communication tradeoff using an event-based approach," in *Proc. Asilomar Conf. Signals, Syst., Comput.*, 2013, pp. 32–36.

[48] D. Shi, T. Chen, and L. Shi, "Event-triggered maximum likelihood state estimation," *Automatica*, vol. 50, no. 1, pp. 247–254, 2014.

[49] Y. Zhang, Z. Wang, L. Zou, and H. Fang, "Event-based finite-time filtering for multirate systems with fading measurements," *IEEE Trans. Aerosp. Electron. Syst.*, vol. 53, no. 3, pp. 1431–1441, Jun. 2017.

[50] J. Morales and Z. Kassas, "Event-based communication strategy for collaborative navigation with signals of opportunity," in *Proc. Asilomar Conf. Signals, Syst. Comput.*, 2018, pp. 548–553.

[51] M. Ouimet, D. Iglesias, N. Ahmed, and S. Martínez, "Cooperative robot localization using event-triggered estimation," *J. Aerosp. Inf. Syst.*, vol. 15, no. 7, pp. 427–449, 2018.

[52] J. Morales, J. Khalife, and Z. Kassas, "Information fusion strategies for collaborative inertial radio SLAM," *IEEE Trans. Intell. Transp. Syst.*, vol. 23, no. 8, pp. 12935–12952, Aug. 2022.
[53] A. Thompson, J. Moran, and G. Swenson, *Interferometry and Synthesis in Radio Astronomy*, 2nd ed. Hoboken, NJ, USA: Wiley, 2001.
[54] M. Shuster, "A survey of attitude representations," *J. Astronautical Sci.*, vol. 41, no. 4, pp. 439–517, Oct. 1993.
[55] S. Kia, B. Van Scoy, J. Cortes, R. Freeman, K. Lynch, and S. Martínez, "Tutorial on dynamic average consensus: The problem, its applications, and the algorithms," *IEEE Control Syst. Mag.*, vol. 39, no. 3, pp. 40–72, Jun. 2019.
[56] J. Farrell and M. Barth, *The Global Positioning System and Inertial Navigation*. New York, NY, USA: McGraw-Hill, 1998.
[57] P. Groves, *Principles of GNSS, Inertial, and Multisensor Integrated Navigation Systems*, 2nd ed. Norwood, MA, USA: Artech House, 2013.
[58] J. Morales and Z. Kassas, "A low communication rate distributed inertial navigation architecture with cellular signal aiding," in *Proc. IEEE Veh. Technol. Conf.*, 2018, pp. 1–6.
[59] Y. Bar-Shalom, X. Li, and T. Kirubarajan, *Estimation With Applications to Tracking and Navigation*. New York, NY, USA: Wiley, 2002.
[60] D. Torrieri, "Statistical theory of passive location systems," *IEEE Trans. Aerosp. Electron. Syst.*, vol. 20, no. 2, pp. 183–198, Mar. 1983.
[61] S. Boyd and L. Vandenberghe, *Convex Optimization*. Cambridge, U.K.: Cambridge Univ. Press, 2004.
[62] R. Snay and M. Soler, "Continuously operating reference station (CORS): History, applications, and future enhancements," *J. Surveying Eng.*, vol. 134, no. 4, pp. 95–104, Nov. 2008.
[63] M. Braasch and A. van Dierendonck, "GPS receiver architectures and measurements," *Proc. IEEE*, vol. 87, no. 1, pp. 48–64, Jan. 1999.
[64] S. Tay and J. Marais, "Weighting models for GPS pseudorange observations for land transportation in urban canyons," in *Proc. Eur. Workshop GNSS Signals Signal Process.*, 2013, pp. 1–4.
[65] J. Liberti and T. Rappaport, "A geometrically based model for line-of-sight multipath radio channels," in *Proc. IEEE Veh. Technol. Conf.*, 1996, vol. 2, pp. 844–848.
[66] M. Maaref and Z. Kassas, "Measurement characterization and autonomous outlier detection and exclusion for ground vehicle navigation with cellular signals," *IEEE Trans. Intell. Veh.*, vol. 5, no. 4, pp. 670–683, Dec. 2020.
[67] M. Maaref, J. Khalife, and Z. Kassas, "Aerial vehicle protection level reduction by fusing GNSS and terrestrial signals of opportunity," *IEEE Trans. Intell. Transp. Syst.*, vol. 22, no. 9, pp. 5976–5993, Sep. 2021.
[68] J. Khalife, K. Shamaei, and Z. Kassas, "Navigation with cellular CDMA signals–Part I: Signal modeling and software-defined receiver design," *IEEE Trans. Signal Process.*, vol. 66, no. 8, pp. 2191–2203, Apr. 2018.
[69] K. Shamaei and Z. Kassas, "LTE receiver design and multipath analysis for navigation in urban environments," *NAVIGATION J. Inst. Navigation*, vol. 65, no. 4, pp. 655–675, Dec. 2018.
[70] K. Shamaei and Z. Kassas, "Receiver design and time of arrival estimation for opportunistic localization with 5G signals," *IEEE Trans. Wireless Commun.*, vol. 20, no. 7, pp. 4716–4731, Jul. 2021.
[71] Z. Kassas and T. Humphreys, "Receding horizon trajectory optimization in opportunistic navigation environments," *IEEE Trans. Aerosp. Electron. Syst.*, vol. 51, no. 2, pp. 866–877, Apr. 2015.
[72] J. Morales and Z. Kassas, "Stochastic observability and uncertainty characterization in simultaneous receiver and transmitter localization," *IEEE Trans. Aerosp. Electron. Syst.*, vol. 55, no. 2, pp. 1021–1031, Apr. 2019.
[73] S. Choi and R. Wette, "Maximum likelihood estimation of the parameters of the gamma distribution and their bias," *Technometrics*, vol. 11, no. 4, pp. 683–690, 1969.
[74] QGP Supply, "GPS active antenna," 2020. [Online]. Available: https://qgpsupply.com/
[75] "Ettus research Tri-band antenna," 2020. www.ettus.com/all-products/vert400
[76] Z. Kassas, J. Khalife, A. Abdallah, and C. Lee, "I am not afraid of the jammer: Navigating with signals of opportunity in GPS-denied environments," in *Proc. 33th Int. Tech. Meeting Satell. Division Inst. Navigation Conf.*, 2020, pp. 1566–1585.
[77] J. Morales and Z. Kassas, "Optimal collaborative mapping of terrestrial transmitters: Receiver placement and performance characterization," *IEEE Trans. Aerosp. Electron. Syst.*, vol. 54, no. 2, pp. 992–1007, Apr. 2018.
[78] K. Pesyna, Z. Kassas, J. Bhatti, and T. Humphreys, "Tightly-coupled opportunistic navigation for deep urban and indoor positioning," in *Proc. 24th Int. Tech. Meeting Satell. Division Inst. Navigation Conf.*, 2011, pp. 3605–3617.
[79] T. Nguyen, G. Mann, A. Vardy, and R. Gosine, "CKF-based visual inertial odometry for long-term trajectory operations," *J. Robot.*, vol. 2020, 2020, Art. no. 7362952.

Joshua J. Morales (Member, IEEE) received the B.S. (High Hons.) degree in electrical engineering from the University of California, Riverside, CA, USA, in 2014, and the Ph.D. in electrical engineering and computer science from University of California, Irvine, CA, USA, in 2020.

He is currently a Principal with StarNav LLC. He was a Member of the Autonomous Systems Perception, Intelligence, and Navigation (ASPIN) Laboratory. His interests include estimation theory, navigation systems, autonomous vehicles, and cyber-physical systems.

Dr. Morales was the recipient of the 2016 Honorable Mention from the National Science Foundation and the 2018 U.S. Department of Transportation Outstanding Graduate Student of the Year award.

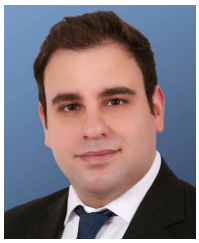

Joe J. Khalife (Member, IEEE) received the B.E. degree in electrical engineering and the M.S. degree in computer engineering from the Lebanese American University, Beirut, Lebanon, and the Ph.D. degree in electrical engineering and computer science from the University of California Irvine, Irvine, CA, USA.

He was a member of the Autonomous Systems Perception, Intelligence, and Navigation (ASPIN) Laboratory. His research interests include opportunistic navigation, autonomous vehicles, and software-defined radio.

Dr. Khalife was the recipient of the 2021 IEEE AESS Robert T. Hill Best Dissertation Award and the 2018 IEEE Walter Fried Award.

Zaher M. Kassas (Senior Member, IEEE) received the B.E. degree in electrical engineering from the Lebanese American University, Beirut, Lebanon, the M.S. degree in electrical and computer engineering from The Ohio State University, Columbus, OH, USA, and the M.S.E. degree in aerospace engineering and the Ph.D. degree in electrical and computer engineering from The University of Texas at Austin, Austin, TX, USA.

He is currently a Professor of electrical and computer engineering with The Ohio State University and the Director of the Autonomous Systems Perception, Intelligence, and Navigation (ASPIN) Laboratory. He is also the Director of the U.S. Department of Transportation Center: CARMEN (Center for Automated Vehicle Research with Multimodal AssurEd Navigation), focusing on navigation resiliency and security of highly automated transportation systems. His research interests include cyber-physical systems, estimation theory, navigation systems, autonomous vehicles, and intelligent transportation systems.

Prof. Kassas was the recipient of the 2018 National Science Foundation (NSF) CAREER Award, the 2019 Office of Naval Research (ONR) Young Investigator Program (YIP) Award, the 2022 Air Force Office of Scientific Research (AFOSR) YIP Award, the 2018 IEEE Walter Fried Award, the 2018 Institute of Navigation (ION) Samuel Burka Award, and the 2019 ION Col. Thomas Thurlow Award. He is a Senior Editor of the IEEE TRANSACTIONS ON INTELLIGENT VEHICLES and an Associate Editor for the IEEE TRANSACTIONS ON AEROSPACE AND ELECTRONIC SYSTEMS and IEEE TRANSACTIONS ON INTELLIGENT TRANSPORTATION SYSTEMS.